# 國立交通大學

## 電子工程學系電子研究所碩士班

## 碩士論文

# III-V 族多接面太陽電池表面光柵收光增益的研究

# The Study of Photon Absorption Enhancement by Surface-Relief Grating on III-V Multi-Junction Solar Cell

研究生：史宜靜

指導教授：林聖迪 博士

中華民國九十九年九月

# III-V 族多接面太陽電池表面光柵收光增益的研究

# The Study of Photon Absorption Enhancement by Surface-Relief Grating on III-V Multi-Junction Solar Cell

研究生：史宜靜　　Student: Yi-Ching, Shih

指導教授：林聖迪　　Advisor: Sheng-Di, Lin

國立交通大學

電子工程學系電子研究所碩士班

碩士論文

A Thesis
Submitted to Department of Electronic Engineering and
Institute of Electronics
College of Electrical and Computer Engineering
National Chiao Tung University
in partial Fulfillment of the Requirements
for the Degree of
Master in Electric Engineering
Sep 2010

Hsinchu, Taiwan, Republic of China

中華民國九十九年九月

# III-V 族多接面太陽電池表面光柵收光增益的研究

學生：史宜靜　　指導教授：林聖迪

國立交通大學

電子工程學系　電子研究所碩士班

## 摘要

本論文主要在於研究如何在 III-V 族太陽能電池表面製作光柵以增廣可利用的太陽光譜頻寬與大角度的吸收。首先我們利用一套嚴格耦合波的數學方法來設計在 AM1.5 下太陽光譜的最佳光柵結構，接著利用電子微影技術將光柵生長在 InGaP/GaAs/Ge III-V 族太陽電池表面；最後進行變角度量測。

量測結果發現，擁有光柵的太陽能電池普遍擁有較高轉換效率，尤其在大角度上的表現，與理論預測的趨勢大致相同。雖然光的吸收率與能量轉換效率並沒有直接關係，但至少我們可以證實擁有光柵的太陽電池卻實在整體效率與大角度的吸收都比只生長抗反射層的電池來得高。故此，如果我們能夠利用低成本的方式大量複製此光柵在太陽能電池上，對於光跡追蹤與其他地面發電運用都有一定的貢獻。

# The Study of Photon Absorption Enhancement by Surface-Relief Grating on III-V Multi-Junction Solar Cell

Student: Yi-Ching Shih    Advisor: Dr. Sheng-Di Lin

Department of Electronics Engineering & Institute of Electronics

National Chiao Tung University

## Abstract

In this dissert, we want to study the improvement of light trapping mechanism due to grating grown its surface in order to achieve higher efficiency at higher incidence. Firstly, we adopt a numerically stable mathematical calculation called rigorous coupled-wave analysis, RCWA, to optimize the profile of grating structure. Then we realize it onto real InGaP/GaAs/Ge III-V MJ solar cell. Lastly, the efficiencies will be measured under standard AM1.5G solar spectrum at various incidences.

In general, the experiment results of samples with grating present higher efficiency than those without. Better performance can also be achieved at larger oblique incidence. Surprisingly, the efficiencies follow the trend of transmittance rate as RCWA has estimated. Although it is quite complicated to judge the relation categorically; we can still attribute the improvements of increasing photon penetrating to grating mechanisms. As a result, if we can find another more effective and less costly way during fabrication process, the contribution of this light trapping structure could be widely extended due to the light tracking system and terrestrial applications have become more prosperous in recent years.

# Acknowledgement (致謝)

回想過去研究的日子，覺得自己何其幸運可以從電物跳到電子所殿堂，然後又是何其幸運進入 MBELab 這大家庭，尤其豐富的資源與周全的設備，讓我研究生涯不用為了排隊等儀器，聽著鳥叫做實驗。我首先要非常感謝我的指導教授 林聖迪博士，當初肯接納我，並選擇讓我嘗試自己的興趣，研究實驗室並不熟悉的領域；最後一年還答應讓我當交換學生去德國開闊視野。雖然我的研究可能不盡理想，但在這懵懂摸索的過程卻收穫滿滿；更加的了解自己、了解做學問的態度、學會獨立思考的價值。也謝謝老師爽朗的胸襟，包容我這有點極端神經質的個性。再來，感謝實驗室大家長 李建平博士，老師的真知灼見常常一針見血的點出我的缺點，嚴師益友的個性，一直是我的表率；謝謝老師常常不吝讚美，讓我更有信心往前走。

還有幫我很多忙的 羅明城學長 凌鴻緒學長 張家華學長 傅英哲學長 潘建宏學長 鄭旭傑學長還有小孟學妹…；一起奮鬥，一起玩耍的憨憨們：賴大師、小豪、歪哥、仁哥、KB、皓皓、小微、阿公、Queena…以後也要一直玩下去唷！還有貼心的柏存、鄭濬。在此也特別感謝許裕彬學長，因為你的鼓勵，讓我撐過很多熬夜的夜晚；祝福你在美國找到自己的一片天，學成歸國。

最後要感謝的就是我的父母，我的家人；一路走來都很支持我做的每項決定，讓我能一無反顧的往前走，還要時常容忍我一觸及發的壞脾氣。能拿到這學位不是偶然，而是建構在很多很多人無私幫忙與鼓勵，在此獻上由衷的感謝，希望大家未來都能快樂健康，並找到自己的興趣勇往直前！

# Contents

# Figure Catalog

## Chapter 1

## Chapter 2

## Chapter 3

## Chapter 4

# Chapter 1

# Introduction

Solar energy absorbed by land and oceans on Earth is over $3.85\times10^{24}\,\mathrm{J}$ in one year. Comparing with the approximate amount of energy $4.87\times10^{20}\,\mathrm{J}$ human needed in a year, it is assumed to be the most renewable green energy in the aspect of environmental protection and has aroused many attentions during crisis of energy shortage in recent years. Many researches have been aiming at finding more sufficient and costless ways to effectively utilize this broadly distributed solar spectrum. III-V multi-junction (MJ) solar cell has long been known for its high conversion efficiencies for its absorption regions can be separated into several subcell among different span of wavelength. Within each subcell, light and be absorbed more effectively without wasting too much photon energy as thermal dissipation than single junction do. Also its efficiency beyond the Shockley-Queisser theoretical limit for single band gap has been achieved. In addition, III-V materials not only obtain direct band gap and high absorption coefficient which shorten the absorption length, it also has the suitable band gap energy which is close to optimum according to theoretical estimation [1].

The dramatic reduction of fabrication cost due to the advancing development technologies makes III-V MJ solar cells attract more attention on both spatial and terrestrial applications. Research studies have been done on either improving lattice disorder and current mismatch on metamorphic material [2-4] or increasing photon flux density within solar cell [5-8]. Many of them have successfully enhanced efficiency by putting textured periodic structure or roughing the surface in the way to optimize the utilization of trapped light. With most of the works had been done on Si based wafer, seldom of researches can be found onto III-V compound solar cell. Therefore, we are interested in investigating surface mechanisms on III-V MJ solar cells. This mechanism has demonstrated to have broadband and oblique anti-reflection characteristics called sub-wavelength surface relief gratings [9-11] by using numerically stable mathematical approach called Rigorous Couple-Wave Analysis (RCWA) which can be applied to solve the surface-relief and multi-layer grating structures [12-15]. In the following chapter we apply RCWA as a tool to optimize the profile of surface relief gratings and realize it by using dielectric materials $SiO_2$ and $Si_3N_4$ onto actual GaAs/InGaP/Ge III-V MJ solar cell.

## 1.1Basic Principle of Solar Cell

### I-V characteristic

Solar cell is a pn junction semiconductor with zero bias applied externally and can deliver electrical power when the generation of electron-hole pairs inside depletion region is swept by internal electric field (figure 1.1). The absorption of photons with energy larger than threshold, the band gap $E_g$, creates electron-hole pairs and generates the output reverse-bias current $I_L$. Figure 1.2 is the schematic photon-generated carrier process inside depletion region. It then produces a forward bias V back onto the cell when passing through the load in which induces the ideal diode current, $I_d$, following the ideal diode equation in forward-bias direction. The total photovoltaic current is referred to as: [16]

$$I = I_L - I_d$$

$$I_d = I_0[\exp(\frac{eV}{kT}) - 1] \tag{1.1}$$

The parameter $I_0$ is defined as ideal reverse saturation bias current.

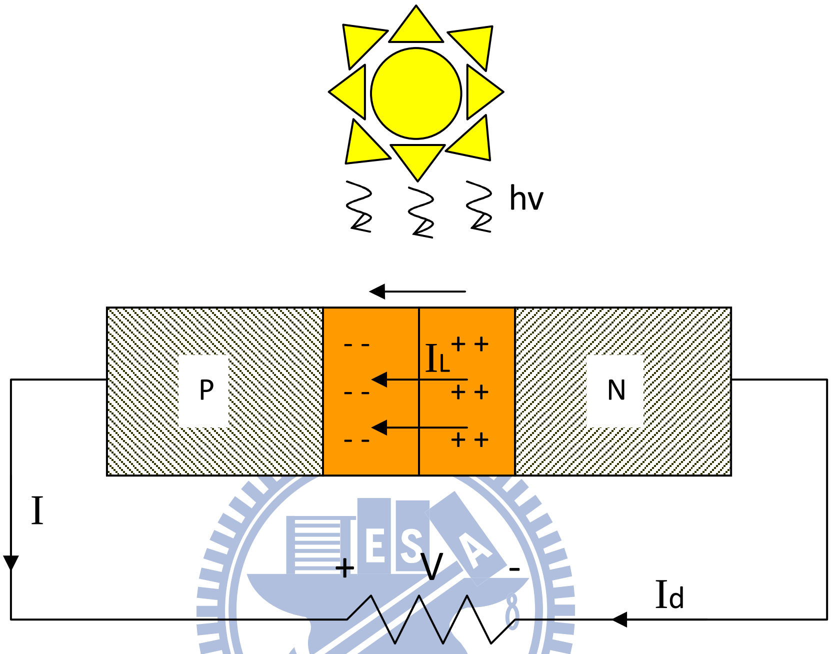

Figure 1.1 The circuit of pn junction solar cell with external load

Figure 1.3 shows the equivalent one diode model circuit inside semiconductor when taking parasitic the series resistance, $R_s$, and shunt resistance, $R_{sh}$, into consideration [17]. The characteristic of ideal diode equation with two resistances can be represented:

$$I = \frac{V - IR_s}{R_{sh}} + I_0\{\exp[\frac{q(V - IR_s)}{kT}] - 1\} \tag{1.2}$$

$R_s$ accounts for the ohmic losses due to metallic contact is usually assumed to be zero in ideal case and $R_{sh}$ relates to the current leakages by defects during process or interconnection is regarded as infinity. By studying the electrical properties allows us to extract more detail parameters of solar cells. Some reports even suggest two-diode model circuit is more suitable in describing the behavior its performance [18,19] which is beyond the scope of our discussion.

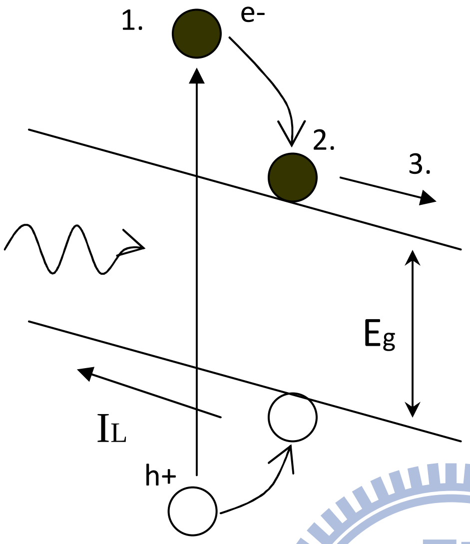

Figure 1.2 Photon-generated carrier process

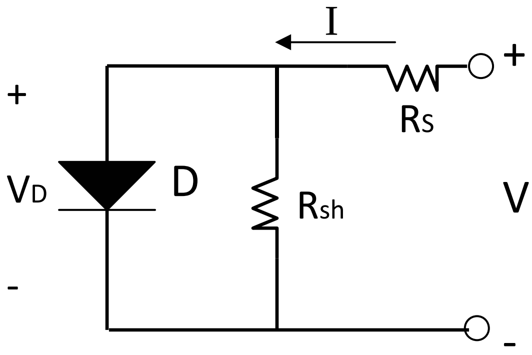

Figure 1.3 Equivalent circuit with parasitic series $R_s$ and shunt $R_{sh}$ resistance

**Standard test condition**

The attenuation of solar spectrum by scattering and absorption of atmosphere is qualified by so called “Air Mass” defined as figure 1.4:

$$\text{AirMass} = \frac{1}{\cos\theta_s} \tag{1.3}$$

The standard test condition (STC) for solar cells is the Air Mass 1.5G spectrum (figure 1.5) designed for flat plate modules. It is a standard terrestrial solar spectrum irradiance distribution developed by American Society for Testing Materials (ASTM) modeled by a sun-facing collector tilt $37^0$ from horizon and the relative light path to the direct solar beam is 1.5 times longer, corresponding to solar zenith angle at $48.19^\circ$. The integrated power density is normalized as

$1000 W / m^2$ at the temperature $25^o C$.

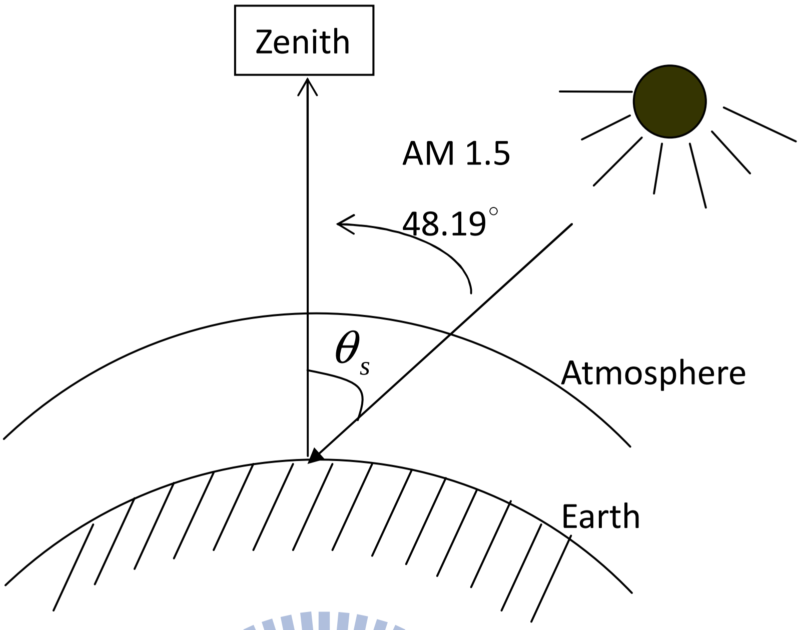

Figure 1.4 Definition of air mass

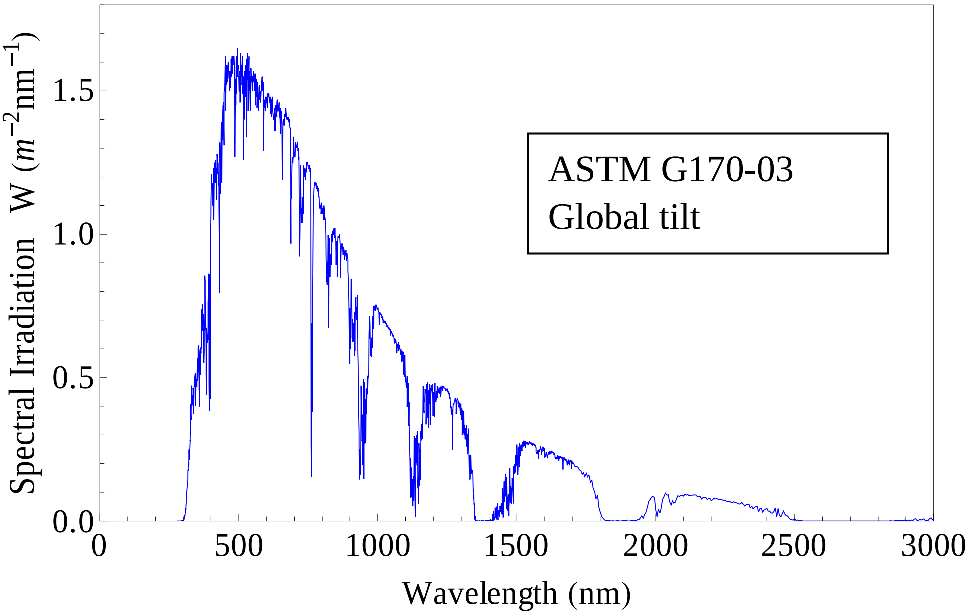

Figure 1.5 ASTM standard of AM 1.5G solar spectrum

## 1.2 Efficiency

### Definition of efficiency

Many papers have discussed about how to improve the efficiency of solar cells based on the basic rule of theoretical calculation, called detailed balance limit. According to W. Shockley and H. J. Queisser [1], if we consider only the ultimate efficiency, $Q_u$ , that each photon with energy greater than band gap, $E_g\,(h\nu_g)$, will contribute one electron without any losing mechanisms. The maximum efficiency can be obtained as the ratio of power delivered by the cell over the solar power impinging onto surface area A.

$$Q_u = \frac{N_p E_g A}{A P_s} \tag{1.4}$$

$$\begin{aligned} N_p &= \text{number of photon with energy greater than } \mathrm{E}_g \\ &= \frac{2\pi}{c^2}\int_{\nu_g}^{\infty}[\exp(\frac{h\nu}{kT_s})-1]^{-1}\nu^2 d\nu \\ P_s &= \text{Solar energy density falling upon device} \\ &= \frac{2\pi h}{c^2}\int_{\nu_g}^{\infty}[\exp(\frac{h\nu}{kT_s})-1]^{-1}\nu^3 d\nu \end{aligned}$$

In real case we have to take other mechanisms, radiation and nonradiation generation or recombination, into account which may generally diminish $Q_u$. In order to improve the efficiency of solar cell, it is necessary to find out the physical function inside each device, thus suggesting possible improvements.

When pn junction solar cell is subjected to radiation, it then produces the photocurrent, $I_L$ in the reverse-bias direction where the ideal diode equation becomes:

$$I = I_L - I_0[\exp(\frac{eV}{kT})-1] \tag{1.5}$$

in which the symbol $I_0$ representing reverse saturation current is resulted from the generation of hole-electron pair due to ambient blackbody temperature T and its own, either nonradiation, $G_{nr}$, or radiation, $G_r$, process. These processes are theoretically independent of external bias. $\frac{kT}{e}$ can be rewritten as a voltage, $V_c$, which is generated by the temperature itself. $I_L$ is also referred to as the short-circuit current, $I_{sh}$, whenever the external bias tends to be zero which is basically generated under illumination, $eG_s$, and the recombination loss in the access of blackbody radiation from the cell, $eR_c$, is also taken into account.

$$\begin{aligned} I_0 &= e(G_r + G_{nr}) \\ I_L &= e(G_s - R_c) \end{aligned} \tag{1.6}$$

Another term of most interest for solar cell is open voltage, $V_{oc}$ which can be obtained by setting $I$ in (1.5) to zero, thus we can obtain.

$$V_{oc} = V_c \ln(1 + \frac{I_L}{I_0}) \tag{1.7}$$

According to theory, the maximum open-voltage can be derived as the band gap voltage $V_g$ as the temperature of the cell approaches zero (1.8). This is resulted from a photon producing an electronic charge with energy $E_g$ can contribute the specific potential energy. Also under this circumstance, no excess generation or recombination process will take place.

$$\lim_{T \to 0} V_{oc} = V_g \tag{1.8}$$

Taking all these mechanisms into the calculation of detail balanced limit of efficiency, we can derive the upper limit of efficiency $\eta$. Conversion efficiency in general is defined as the ratio of maximum power that a cell can deliver to a matched load over total incident power, $P_s$, from the sun.

$$\eta = \frac{I_m V_m}{P_s} = \frac{I_{sh} V_{oc}.FF}{P_s} \qquad (1.9)$$

It is shown in figure 1.6 where $I_m$ and $V_m$ is the current density and voltage of maximum output power. Filling factor, FF, defined as $I_m V_m / I_{sh} V_{oc}$ is also a key measurement of solar cell performance and typically is around 0.7~0.8.

### Improvement of efficiency

Detail balanced limit requires the following assumptions: (1)The probability, $f$, of a photon with energy greater than $E_g$ that will produce a hole-electron pair must be unity;(2) Only radiative recombination mechanism is required;(3) The charges are completely separated and transported to external circuit without loss. Figure 1.7 shows the theoretical efficiency calculated with cell and sun temperatures at 300K and 6000K respectively [1]. Curve f assumes all the assumption above to be ideal and the incident angle subtended by the sun upon solar cell to be normal. Other curves decrease gradually from curve g to i. as $f$ less than unity or larger the incident angle. This indicates the maximum efficiency is approximately 31% which corresponds to an energy gap value around 1.3~1.4eV.

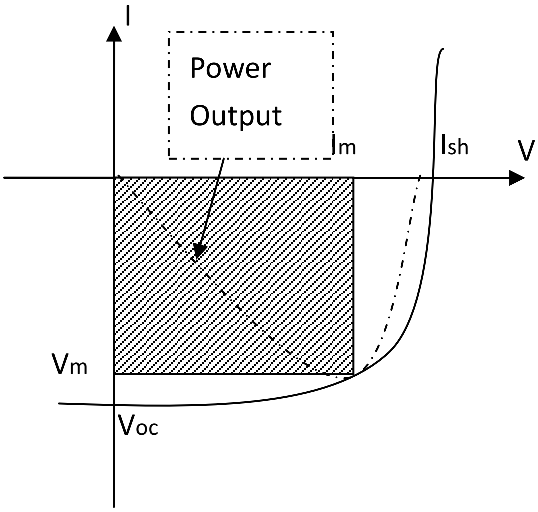

Figure 1.6 The current voltage and power output diagram of solar cell

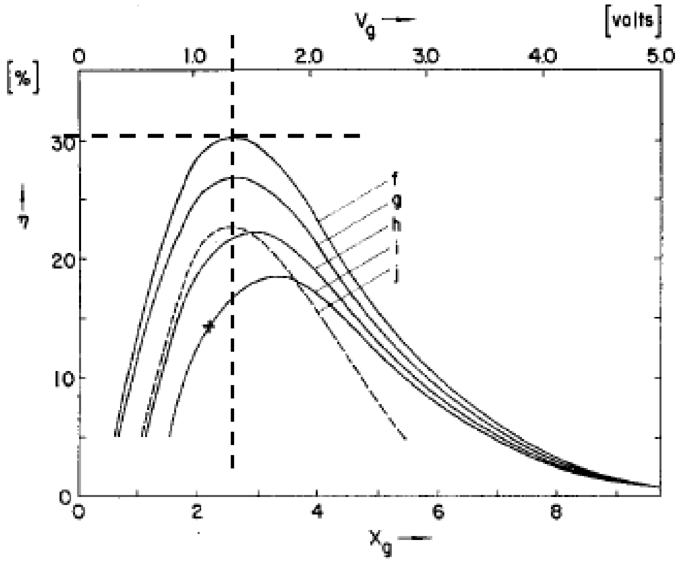

Figure 1.7 Detailed balanced limit of solar efficiency

Equation (1.9) can be redefined in terms of ultimate efficiency (1.4) as below:

$$\eta = Q_u . FF . f . \frac{V_{oc}}{V_g} \tag{1.10}$$

Actual device do not obey the ideal relationship curves in figure 1.7. The reasons for these deviations come from the last three terms in equation (1.10). Many researches have been studied and published to deal with these questions and some methods based on the basic physical concept can be done by focusing on the assumptions presumed:

(1) Only single junction is concerned. This can be solved by increasing the number of band gap such as to parcel out the preferable wavelength into each subcell corresponding to different band gaps. Multi-junction (multi-band) solar cells have the potential of achieving high efficiency over 53.6% theoretically

(2) Photon flux density depends only on the temperature of sun and the angle of light subjecting on cell. The concentration light increases the geometrical factor, $F_s$, and widens the angular range from $\theta_s$ to $\theta_c$ subtended by sun, thus enhancing the total flux intensity by S [17].

$$S = \frac{\sin^2 \theta_c}{\sin^2 \theta_s} \tag{1.11}$$

(3) Increase the number of electron-hole pair that each photon can create. This requires the mechanism called impact ionization.

(4) Some fraction of incident light will be reflected from the surface of cell, $R$, and others will pass inside but attenuate exponentially along the way. Unless there is any chance to diminish the reflection from the surface toward zero and absorb each incident photon perfectly, the probability of gaining one electron-hole pair per photon, $f$, would never approach unity and the equation (1.10) would never attain ultimate target. Therefore, the following equation about $f$ should be considered.

$$f = (1 - R)(1 - e^{-\alpha x}) \tag{1.12}$$

$\alpha$ is the absorption coefficient of the cell. If the $\alpha$ is large, the photons are absorbed over a relatively short distance.

(5) Another problem has not been considered is about how to harness the excess kinetic energy of the photo-generated carriers over band gap before they dissipate into thermal energy which increases the possibilities of other non-radiation recombination, Auger recombination for instance. The idea of hot carrier solar cell then comes up with the solution to recycle this excess energy but the effect is still under investigation [20].

Practical methods are still being done with regard to enhancing the presumptive analysis toward ideal expectation. The first two strategies are more commonly used in the III-V multi-junction solar cells (figure 1.9) and further discussion about (4) is in section, 1.4.

## 1.3 Multi-junction Solar Cells

Detail balanced theory estimates the upper limit of single junction where only a narrow range of specific wavelength can be absorbed. On the contrary, multi-junction (MJ) solar cells consisting of multiple subcells with different bandgaps can efficiently convert broadband of photon energy in to photocurrent so their efficiency can beat up cells with single junction.

In 1990, Fraas group invented a two junction mechanically stacked AlGaAs/ GaAs solar cell and achieved over 35% efficiency [21]. But this kind of devices though was estimated to have higher conversion efficiency due to fewer defects between the connections of two subcells, it requires individual circuit for each subcell, which makes the processing more complicated. Therefore, over the pass few decades, there have been great improvements for monolithic cascaded junction solar cell [22,23]. The achievements of low-loss tunnel junction between two or more interconnection of cells and the largely reduced lattice or current mismatch make monolithic cascaded solar cell more realistic and popular in recent years.

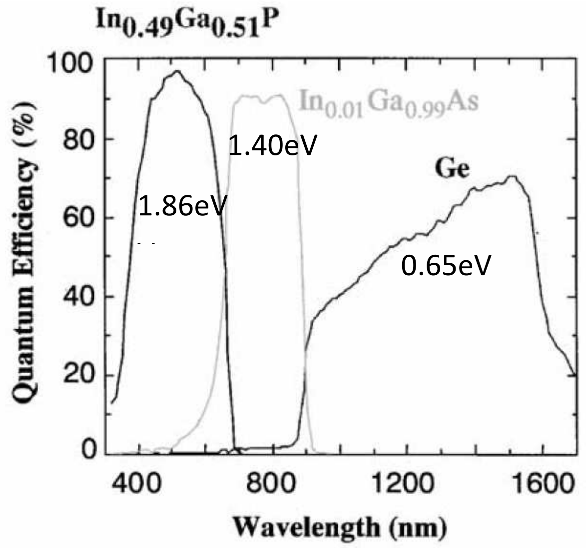

Figure 1.8 Spectrum response of GaInP/GaInAs/Ge MJ solar cell

III-V MJ solar cell has long been known to have theoretical potential of reaching ultrahigh efficiency over 40%. A record of surpassing 40.8% by metamorphic GaInP/GaInAs/Ge solar cell (figure1.9) had been achieved recently [4]. Figure 1.8 shows the spectrum response of GaInP/GaInAs/Ge MJ solar cell and the schematic cell structure with its equivalent model circuit in is shown in figure 1.9. Obviously, it divides solar spectrum into three parts which nearly covers the main energy distribution. The development of optically and electrically low-loss tunnel junction is realized and the band diagram can be schematically shown in figure 1.10 [3]. Higher photon energy is mainly extracted by InGaP top subcell, medium energy by GaAs in the middle and lowest energy by Ge at the bottom. Where we can notice the formation of thin and wide-band-gap tunnel junction is a crucial issue to realize high-efficiency MJ solar cells. Although MJ solar cells are mostly used for space application, the investigations for its terrestrial applications have begun to attract more attentions in recent years.

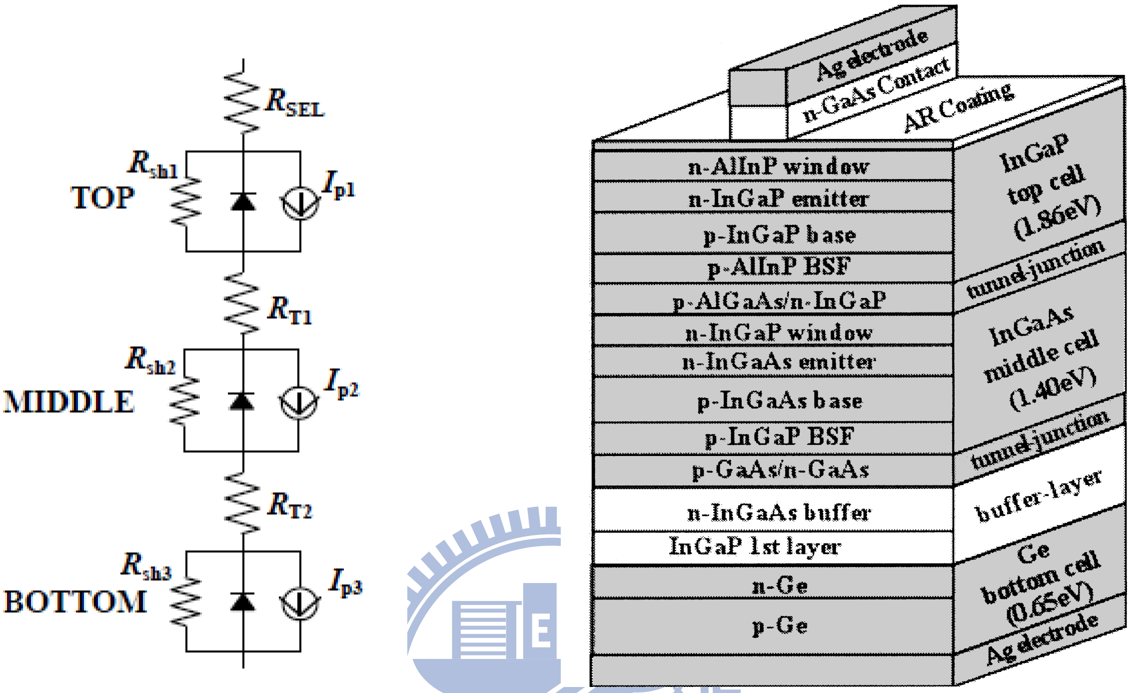

Figure 1.9 Schematic GaInP/GaInAs/Ge structure, right, and equivalent circuit, left.

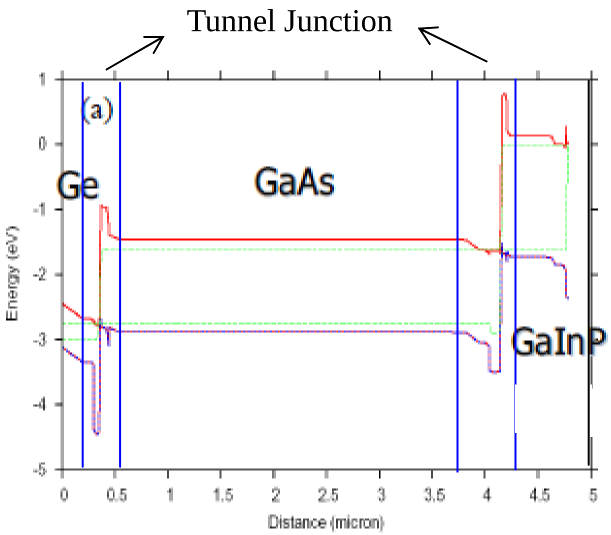

Figure 1.10 Band diagram of GaInP/GaInAs/Ge solar cell

## 1.4 Minimizing Reflection

In order to maximize the optical absorption in achieving high performance solar cells, many solutions have been demonstrated about how to diminish the reflection on the surface over extensive spectrum range. Various anti-reflection coatings (AR) are widely utilized by growing a thin film of dielectric layer on the front of surface but that can only reduce the reflectivity at certain specific wavelength and are also restricted on narrow angle of incidence.

In 1880, Lord Rayleigh first mathematically calculated the "graded refractive index layer" contain broadband anti-reflection characteristic and, in 2007, Martin's group had reported that an oblique-angle deposition of $TiO_2$ and $SiO_2$ coating [6] (figure 1.11) has low reflectivity over the entire visible and near infrared spectrum. At the same time, another group demonstrated a new microscale surface texturing on solar cell in the shape of spherical (figure 1.13) and proposed to be an omni-directional anti-reflection coating [5] accompanying mathematical calculation called rigorous coupled wave analysis (RCWA).

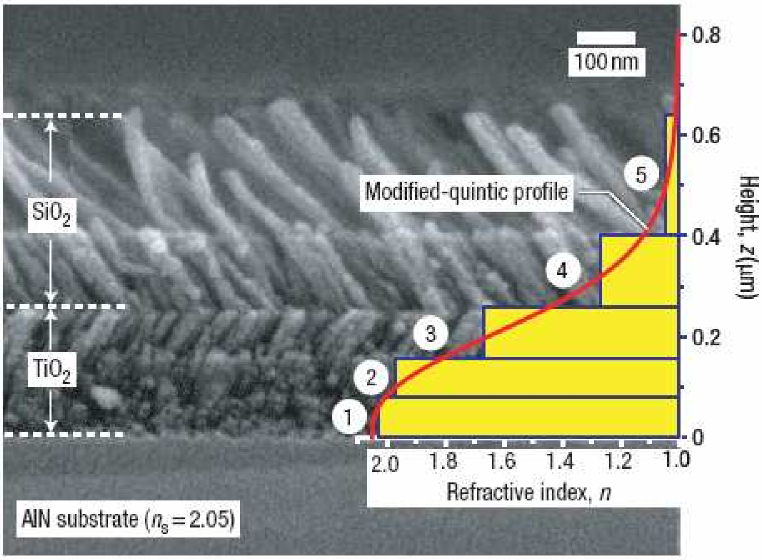

Figure 1.11 The cross section SEM image of graded-index coating

Figure 1.12 Spherical particles of omnidirectional ARC

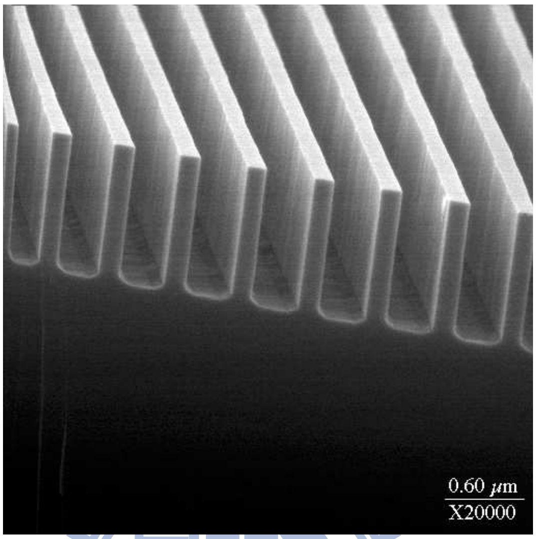

Figure 1.13 The cross section SEM image of 1D rectangular grating

However, different attempts have been studied for the structures of AR over broadband spectrum, sub-wavelength surface-relief grating (figure 1.12) has also been long investigated to have such broadband absorption characteristic [9,24,25]. At larger propagation angles, most of the light is coupled into higher transmitted diffraction order which enhance the absorption length and extensively increase the generation of electron-hole pairs. Although the advantage of sub-wavelength grating is proposed, it still has not yet been fabricated on the ultrahigh efficiency III-V triple junction solar cells.

Before the grating structure experimentally make on a real III-V triple junction solar cell, the numerical mathematics RCWA will be briefly discussed and treated as a numerical analysis approach during the whole optimum and ideal simulations in the following chapter.

# Chapter 2

# Rigorous Couple-Wave Analysis Theory and Coding

## 2.1 Basic Concept of RCWA

### Grating equation

The principle of constructive interference only exists when the light scattered in phase which means the path difference equals the multiple of wavelength. The concept can be visualized in figure 2.1 and expressed in a simple equation (2.1), called the grating equation.

$$\Lambda \sin\theta_m - \Lambda \sin\theta_i = m\lambda \qquad m = 0, \pm 1, \pm 2.... \tag{2.1}$$

m number the order of diffractive wave. This can transform into another more general form in terms of wavevector, k, in the direction of x, called Floquent condition:

$$k_{mx} = k_{Ix} + mK \qquad K = \frac{2\pi}{\Lambda} \tag{2.2}$$

$\Lambda$ represents the grating period, $k_{Ix}$ and $k_{mx}$ are the x component of m order

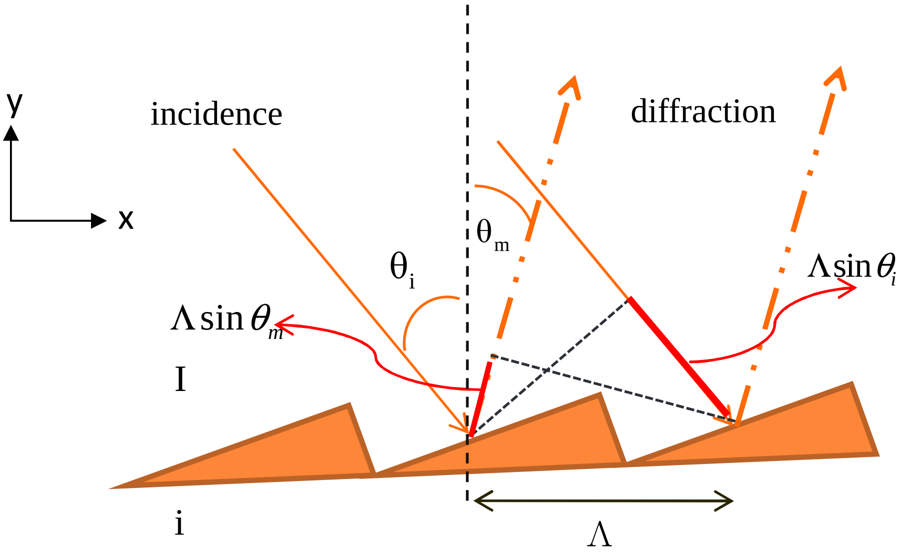

Figure 2.1 Schematic interpretation of grating principle

wavevector in incident region I and transmission region. K can be called grating vector. Figure 2.2 shows the schematic Floquent condition (2,2) between two media in vector space. The radius is the amplitude of propagating wavevector. Only a limited number order of wave can exist depending on the subtraction and addition of grating vector.

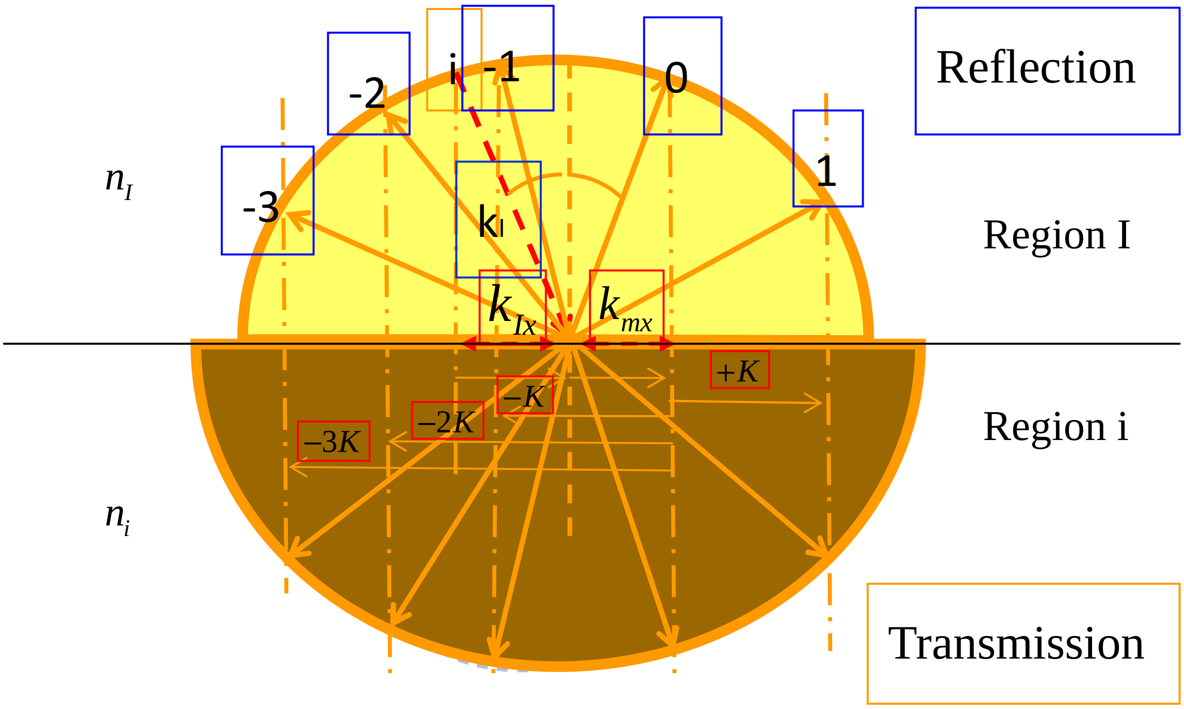

Figure 2.2 Floquent equation in wavevector space

Sub-wavelength surface relief grating is a kind of diffraction structure in the scale of wavelength that mostly produce zero order and all higher order propagate as evanescent wave. In 1D grating, it sets the maximum limit on the maximum grating period as $\lambda_0$ being the vacuum wavelength [9]:

$$\Lambda \le \frac{\lambda_0}{n_I \sin\theta_i + n_i} \tag{2.3}$$

### RCWA formulism

RCWA is one of the numerical solutions being widely applied and studied in the interest of dealing with diffractive characteristics of electromagnetic waves on dielectric gratings. It expands the resolution wave in the form of plane wave components, and the amplitude of each component are obtained by matching the boundary conditions between two refractive materials.

In the general case of one-dimensional rectangular grating (figure 2.3), the grating vector is parallel to x direction and filling factor is defined as the ratio of width of rectangular over period.

$$\text{Filling Factor} = \frac{W}{\Lambda} \tag{2.5}$$

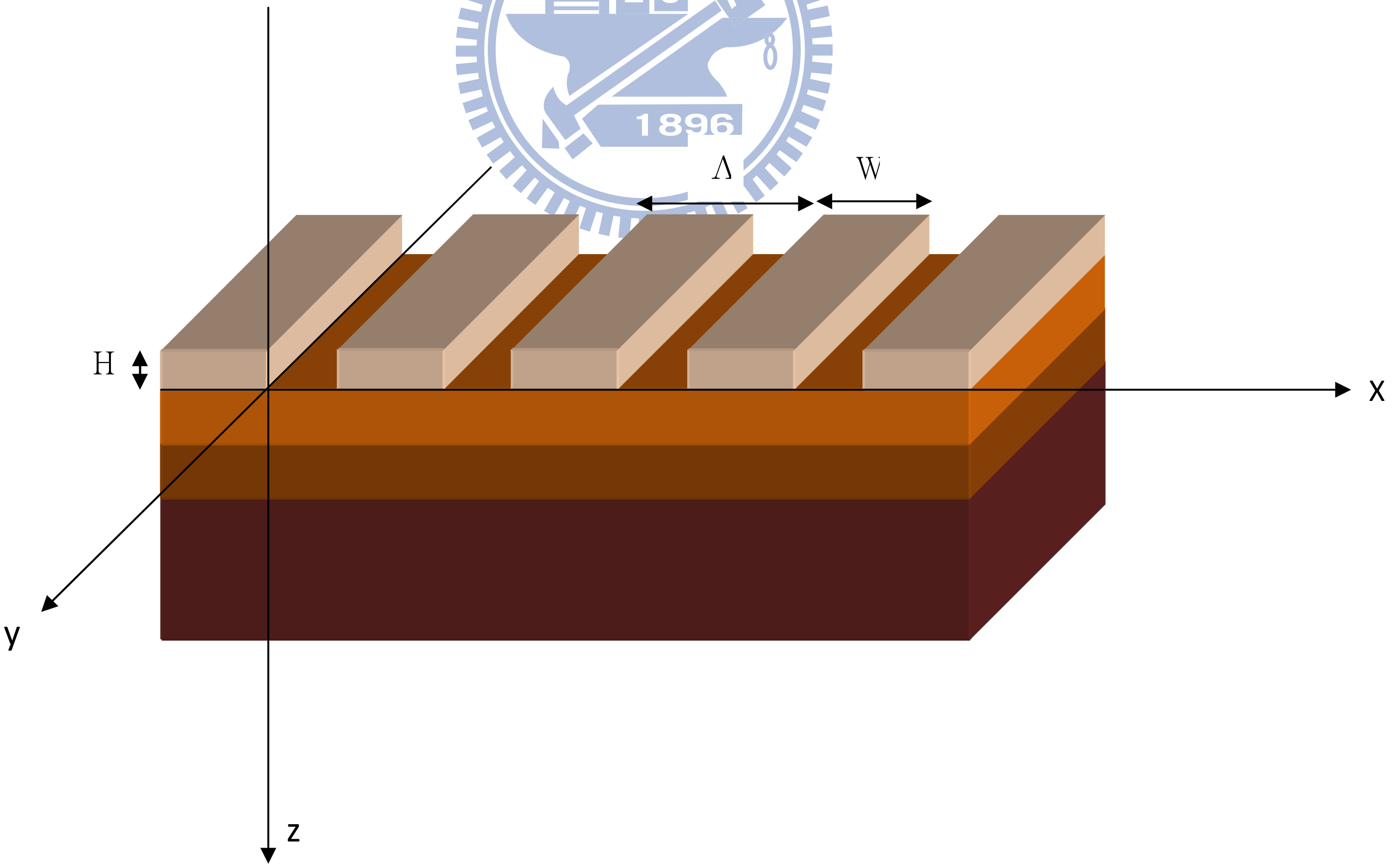

Figure 2.3 Schematic diagram of 1-D grating structure

For the case of planar diffraction solution, electromagnetic wave can be easier to deal with by decomposing into TE and TM polarization, where electric and magnetic field are normal to the plane of incidence (x-z plane) respectively. TE and TM wave can be handled individually. Here we briefly present the formulation of TE polarization. The extension of TM problem is straightforward, thus it is not mentioned below.

**TE component**

Sub-wavelength gratings has been theoretically proved to obtain the homogeneous properties [10, 24], thus Maxwell's equation can be described in the form of (2.6), with electromagnetic boundary conditions as (2.7) [27]

Maxwell's equation in linear and homogeneous media

$$\begin{cases} (i)\quad \nabla\cdot E=\dfrac{\rho}{\varepsilon} & (iii)\quad \nabla\times\vec{E}=-\dfrac{\partial B}{\partial t} \\ (ii)\ \nabla\cdot B=0 & (iv)\quad \nabla\times H=J_f+\varepsilon\dfrac{\partial E}{\partial t} \end{cases} \tag{2.6}$$

Accompany with the Boundary Condition below

$$\begin{cases} (i)\quad E_{\perp}^{I}-E_{\perp}^{II}=\dfrac{\sigma_f}{\varepsilon} & (iii)\ E_{//}^{I}-E_{//}^{II}=0 \\ (ii)\ B_{\perp}^{I}-B_{\perp}^{II}=0 & (iv)\ H_{//}^{I}-H_{//}^{II}=K_f\times\hat{n} \end{cases} \tag{2.7}$$

Where $\hat{n}$ is unit vector with the direction normal to grating surface. $\rho$ is the free charge, $\sigma_f$ the surface free charge density, $K_f$ the surface free current and $J_f$ the free volume current density. Those values mentioned above in dielectric materials are generally treated as zero. $\varepsilon$ is the relative permittivity. (2.6) satisfies the Maxwell's equation in differential form:

$$\frac{\partial E_y}{\partial z}=j\mu\omega H_x \qquad \frac{\partial E_y}{\partial x}=\ j\mu\omega H_z \qquad \frac{\partial H_x}{\partial z}=\ j\varepsilon\omega E_y+\frac{\partial H_z}{\partial x} \tag{2.8}$$

As for TE polarization, incident electric field $E_y$ in y direction is expanded into summation of total diffractive waves from region I to II which are schematically shown within the unit cell of periodic structure in figure 2.4.

Region I $(z > 0)$:

$$E_{I,y} = \exp[-jk_I\vec{r}\,] + \sum_{i=1}^{n} R_i \exp[-j(k_{I,xi}x - k_{I,zi}z)]$$

Region d layer $(0 < z < L)$:

$$E_{d,y} = \sum_{i=1}^{n} F_i \exp\{-j[k_{d,xi}x - k_{d,zi}(z - l_{d-1})]\} + \sum_{i=1}^{n} B_i \exp[-j(k_{d,xi}x + k_{d,zi}(z - l_d)]$$

$$= \sum_{i=1}^{n} S_{d,yi}(z)\exp[-jk_{d,xi}x]$$

$$H_{d,y} = -j/\omega\mu \sum_{i=1}^{n} U_{d,xi}(z)\exp[-jk_{d,xi}x]$$

$$l_d = \sum_{d=1}^{m} h_d$$

Region II $(z < L)$:

$$E_{II,y} = \sum_{i=1}^{n} T_i \exp\{-j[k_{II,xi}x + k_{II,zi}(z - L)]\} \qquad (2.9)$$

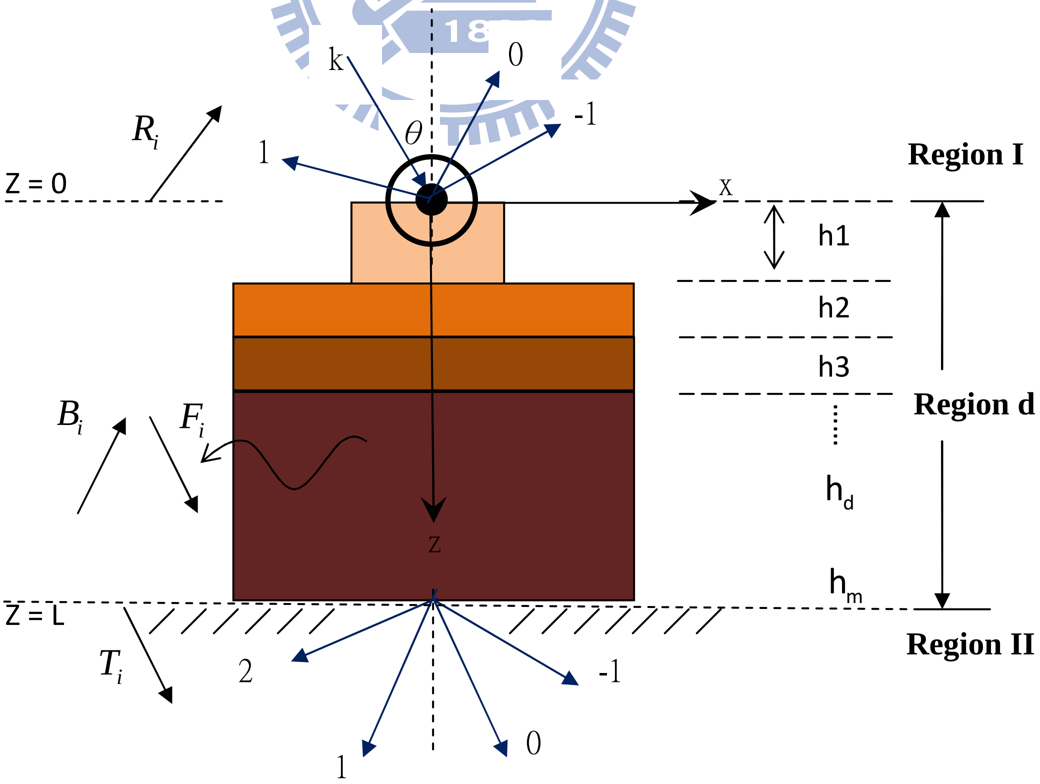

Figure 2.4 TE diffraction within 1D grating structure unit cell

$F_i$ and $B_i$ are the forward and backward amplitudes of reflected and transmitted wave in each layer. $R_i$ and $T_i$ can be derived by solving tangential wave continuity of each interface systematically by means of boundary conditions (2.7). n is the number of harmonics field in Fourier expansion.

Substitute grating formula (2.2) into (2.9) and summarize into Maxwell's equation (2.8). We obtain the coupled wave equations:

$$\begin{aligned} \frac{\partial S_{d,yi}}{\partial z} &= k_0 U_{d,xi} \\ \frac{\partial U_{d,xi}}{\partial z} &= \left(\frac{k_{d,xi}^2}{k_0}\right) S_{d,yi} - k_0 \sum_{p=1}^{n} \varepsilon_{i-p} S_{d,yp} \end{aligned} \tag{2.10}$$

$\mathrm{S}_{d,yi}$ and $\mathrm{U}_{d,xi}$ are normalized harmonic field for electric and magnetic wave respectively. $\mathrm{k}_0$ represents the wave vector in free space. $\varepsilon(\mathrm{x})$ is expanded in Fourier expansion.

$$\begin{aligned} \varepsilon(\mathrm{x}) &= \sum_{p=1}^{n} \varepsilon_p \exp\left[j \frac{2\pi p}{\Lambda} x\right] \\ \varepsilon_p &= (n_d^2 - n_{d+1}^2) \frac{\sin(\pi p f)}{\pi p} \end{aligned} \tag{2.11}$$

Where $n_d$ the refractive index in layer d. is $f$ is the filling factor defined in (2.5). To combine (2.11) into (2.10) differential equation, we can set up a simple matrix form. (2.12)

$$\begin{pmatrix} \partial_z S_{d,y1} \\ \partial_z S_{d,y2} \\ . \\ . \\ . \\ \partial_z S_{d,yn} \end{pmatrix} = k_0 \begin{pmatrix} U_{d,y1} \\ U_{d,y2} \\ . \\ . \\ . \\ U_{d,yn} \end{pmatrix}$$

$$\begin{pmatrix} \partial_z U_{d,x1} \\ \partial_z U_{d,x2} \\ . \\ . \\ . \\ \partial_z U_{d,xn} \end{pmatrix} = \frac{1}{k_0} \begin{pmatrix} k_{x1}^2 & 0 & 0 & 0 \ldots. \\ 0 & k_{x2}^2 & 0 & 0 \ldots. \\ 0 & 0 & k_{xi}^2 & 0 \ldots. \\ \vdots & \vdots & \vdots & \\ & & & k_{xn}^2 \end{pmatrix} \begin{pmatrix} S_{d,y1} \\ S_{d,y2} \\ . \\ . \\ . \\ S_{d,yn} \end{pmatrix} - k_0 \begin{pmatrix} \varepsilon(0) & \varepsilon(-1) & \varepsilon(-2) \ldots \varepsilon(1-n) \\ \varepsilon(1) & \varepsilon(0) & \varepsilon(-1) \ \ldots \varepsilon(2-n) \\ \varepsilon(2) & \varepsilon(1) & \varepsilon(0) \ \ \ldots \varepsilon(3-n) \\ \varepsilon(i) & \varepsilon(i-p) & \ldots \varepsilon(i-n) \\ \vdots & & \\ \varepsilon(n) & & \varepsilon(0) \end{pmatrix} \begin{pmatrix} S_{d,y1} \\ S_{d,y2} \\ . \\ . \\ . \\ S_{d,yn} \end{pmatrix}$$

$$\rightarrow \begin{pmatrix} \dfrac{\partial^2 S_{d,1}}{\partial z^2} \\ \dfrac{\partial^2 S_{d,2}}{\partial z^2} \\ . \\ . \\ \dfrac{\partial^2 S_{d,n}}{\partial z^2} \end{pmatrix} = k_0 \underbrace{\begin{pmatrix} \dfrac{k_1^2}{k_0^2} & 0 & 0 & 0 & \cdots \\ 0 & \dfrac{k_2^2}{k_0^2} & 0 & 0 & \cdots \\ \vdots & & & & \\ & & & & \dfrac{k_n^2}{k_0^2} \end{pmatrix}}_{K^2} \begin{pmatrix} S_{d,y1} \\ S_{d,y2} \\ . \\ . \\ . \\ S_{d,yn} \end{pmatrix} - k_0 \underbrace{\begin{pmatrix} \varepsilon(0) & \varepsilon(-1) & \varepsilon(-2) \ldots \varepsilon(1-n) \\ \varepsilon(1) & \varepsilon(0) & \varepsilon(-1) \ \ldots \varepsilon(2-n) \\ \varepsilon(2) & \varepsilon(1) & \varepsilon(0) \ \ \ldots \varepsilon(3-n) \\ \varepsilon(i) & \varepsilon(i-p) & \ldots \varepsilon(i-n) \\ \vdots & & \\ \varepsilon(n) & & \varepsilon(0) \end{pmatrix}}_{E} \begin{pmatrix} S_{d,y1} \\ S_{d,y2} \\ . \\ . \\ . \\ S_{d,yn} \end{pmatrix}$$

$$\rightarrow \begin{cases} \left(\dfrac{\partial^2 S_{d,yi}}{\partial z^2}\right) = k_0 \left(K^2 - E\right)\left(S_{d,yi}\right) \\ \left(\dfrac{\partial^2 U_{d,xi}}{\partial z^2}\right) = k_0 \left(K^2 - E\right)\left(U_{d,xi}\right) \end{cases} \tag{2.12}$$

By calculating the eigenvector and eigenvalue of equation (2.12) and matching the boundary condition in (2.7) between adjacent layers, we can set up a series of related equations and summarize them in a clear and tidy matrix form in the list below. More detailed formulations are reported in paper [14-16].

**Full mathematic formulation for surface-relief grating**

| Region I | |
|---|---|
| TE | TM |
| $\begin{pmatrix}\delta_{i0}\\ j\delta_{i0}\cos\theta\end{pmatrix}+\begin{pmatrix}I\\ -jY_I\end{pmatrix}R=\begin{pmatrix}W_1 & W_1X_1\\ V_1 & -V_1X_1\end{pmatrix}\begin{pmatrix}C_1^+\\ C_1^-\end{pmatrix}$ | $\begin{pmatrix}\delta_{i0}\\ j\dfrac{\delta_{i0}\cos\theta}{n_I}\end{pmatrix}+\begin{pmatrix}I\\ -jZ_I\end{pmatrix}R=\begin{pmatrix}W_1 & W_1X_1\\ V_1 & -V_1X_1\end{pmatrix}\begin{pmatrix}C_1^+\\ C_1^-\end{pmatrix}$ |
| Region ℓ to ℓ -1 | |
| $\begin{pmatrix}W_{l-1}X_{l-1} & W_{l-1}\\ V_{l-1}X_{l-1} & -V_{l-1}\end{pmatrix}\begin{pmatrix}C_{l-1}^+\\ C_{l-1}^-\end{pmatrix}=\begin{pmatrix}W_l & W_lX_l\\ V_l & -V_lX_l\end{pmatrix}\begin{pmatrix}C_l^+\\ C_l^-\end{pmatrix}$ | |
| Region II | |
| $\begin{pmatrix}W_LX_L & W_L\\ V_LX_L & -V_L\end{pmatrix}\begin{pmatrix}C_L^+\\ C_L^-\end{pmatrix}=\begin{pmatrix}I\\ jY_{II}\end{pmatrix}T$ | $\begin{pmatrix}W_LX_L & W_L\\ V_LX_L & -V_L\end{pmatrix}\begin{pmatrix}C_L^+\\ C_L^-\end{pmatrix}=\begin{pmatrix}I\\ jZ_{II}\end{pmatrix}T$ |

Table 2.1 Summary of full mathematic formulation for RCWA

Reflected and diffracted amplitudes are determined simultaneously by solving table 2.1 in either TE or TM mode. Another simpler and memory saving way is called partial solution approach. It employs the same concept of full mathematics method in a much more stable and efficient way with only half number of matrix multiplications needed comparing to full-solution approach. By solving the reflected and transmission diffraction mode separately, the size of matrix can also decrease into half. The partial solution formulism is listed in Table 2.2. Further deductions from Table 2.1 to Table 2.2 are proved in Appendix.

**Partial mathematic formulation for surface-relief grating**

| | Transmission Formulism | Reflection Formulism |
|---|---|---|
| TM | $\begin{pmatrix} f_L \\ g_L \end{pmatrix} C_L^{+} + \begin{pmatrix} y_L \\ z_L \end{pmatrix} = \begin{pmatrix} I \\ jZ_{II} \end{pmatrix} T$ | $\begin{pmatrix} f_1 \\ g_1 \end{pmatrix} C_1^{+} = \begin{pmatrix} \delta_{io} \\ j\dfrac{\delta_{i0}\cos\theta}{n_I} \end{pmatrix} + \begin{pmatrix} I \\ -jZ_I \end{pmatrix} R$ |
| TE | $\begin{pmatrix} f_L \\ g_L \end{pmatrix} C_L^{+} + \begin{pmatrix} y_L \\ z_L \end{pmatrix} = \begin{pmatrix} I \\ jY_{II} \end{pmatrix} T$ | $\begin{pmatrix} f_1 \\ g_1 \end{pmatrix} C_1^{+} = \begin{pmatrix} \delta_{io} \\ jn_I\delta_{i0}\cos\theta \end{pmatrix} + \begin{pmatrix} I \\ -jY_I \end{pmatrix} R$ |

Table 2.2 Summary of partial mathematic formulation for RCWA

## 2.2 Formulism in Computational Algorithm

$$\text{Tsolar} = \frac{\sum_i^n \int_{0.3}^{2} \mathrm{T}_i(\lambda)\mathrm{Solar}(\lambda)\, d\lambda}{\int_{0.3}^{2} \mathrm{Solar}(\lambda)\, d\lambda} \qquad (2.13)$$

TSolar is defined as the ration of power penetrating at all diffraction orders over power incidence throughout wavelength of interest from 0.3um to 2um where GaInP/GaInAs/Ge solar cell dominates. Our goal is to find out the configuration for grating with highest Tsolar under 6000K solar spectrum. We then compile partial solution approach into mathematic software (Mathematica) and set up all the matrix formula in Table 2.2. The algorithm used to extract the optimized results utilized iterative method. Table 2.3 shows the computational process.

## Computational algorithm

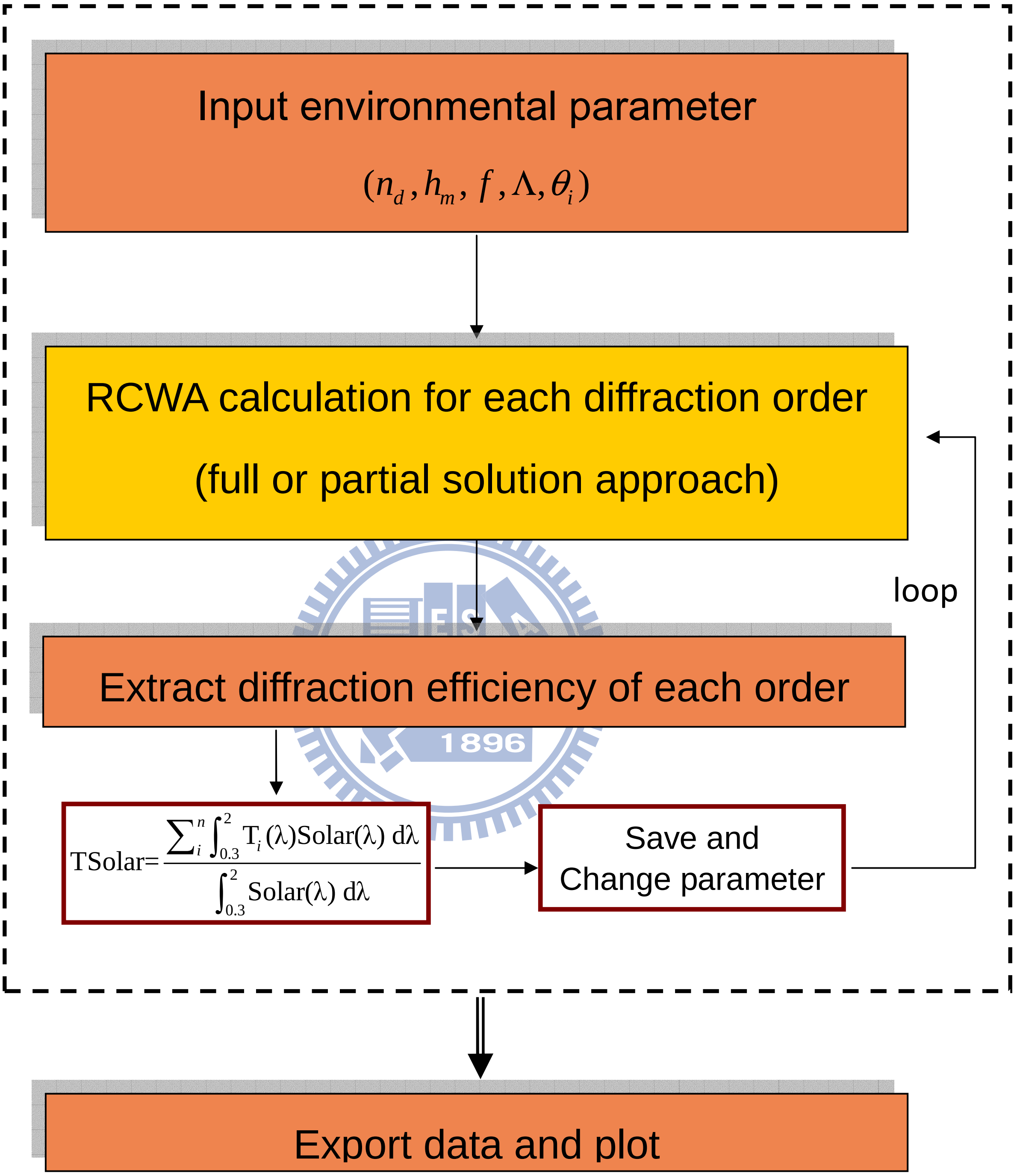

Table 2.3 Computational algorithm diagram

# Chapter 3

# Simulation Results and Analysis

## 3.1 Anti-Reflection Coating

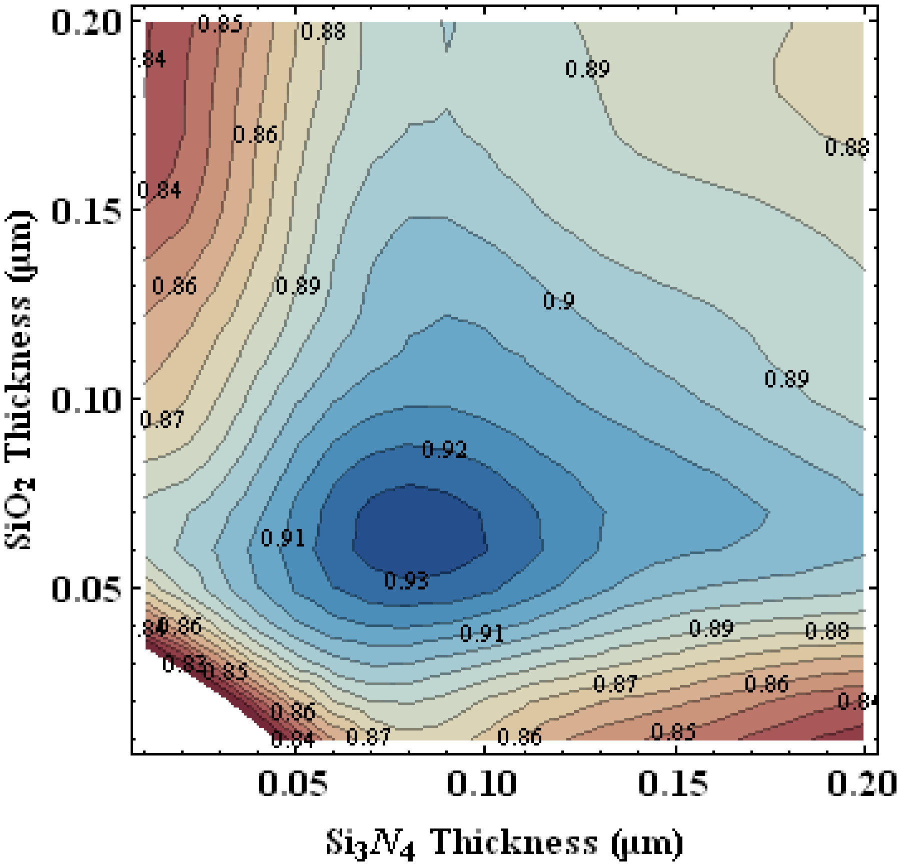

Figure 3.1 Contour map of transmittance under standard solar spectrum as functions of $SiO_2$ and $Si_3N_4$ thickness

We first design the anti-reflection coating (AR) using the program discussed in previous chapter, and assume TE and TM polarization being equally the same at normal incidence. Double-layer of $SiO_2$ and $Si_3N_4$ AR were adopted with refractive its index 1.54 and 2, respectively. $SiO_2$ has lower refractive index that is closer to the refractive index of air 1, therefore it is chose to stack on top. Also the refractive index for the substrate is 3.5.

The result is shown in figure 3.1, a contour map of Tsolar as function of $SiO_2$ and $Si_3N_4$ thickness. This figure shows that maximum occurs at the range where thickness of $SiO_2$ and $Si_3N_4$ layers locate around 80 nm and 60 nm, respectively, with transmitted efficiencies over 93%. Although transmitted wavelength distribution of AR does not center at main peak of solar spectrum near 500 nm to 700 nm (figure 3.2), the total TSolar compared with no AR can still improve from 70%, to as high as 93.6%.

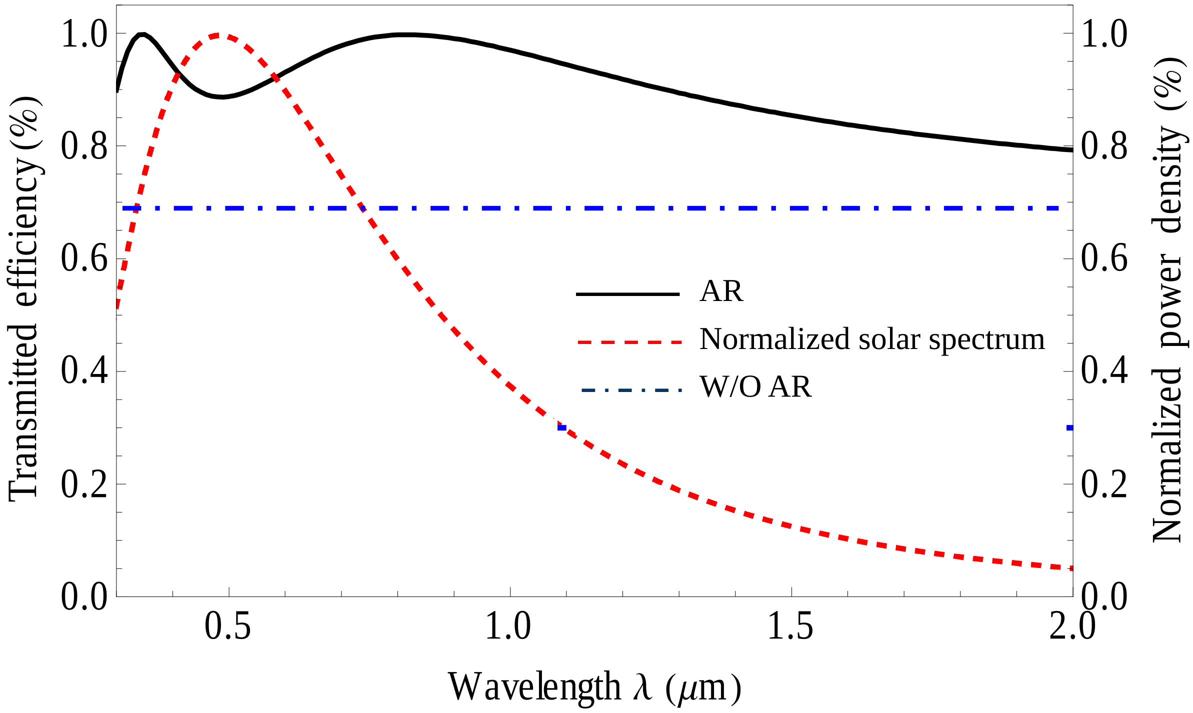

Figure 3.2 The comparison of surface transmittance with and without AR to normalized black body power density at 6000K

Figure 3.2 shows the comparison distribution of transmittance for surface with and without AR to normalized power density of black body radiation at 6000K as function of wavelength. Apparently, the total transmittance has been broadly improved.

## 3.2 Sub-Wavelength Grating Structure

AR though well performs at normal incidence; it works only at a certain span of wavelength and incident angle. However, broad band characteristic of grating structure has been investigated and widely employed to the enhancement of light collection at oblique angle.

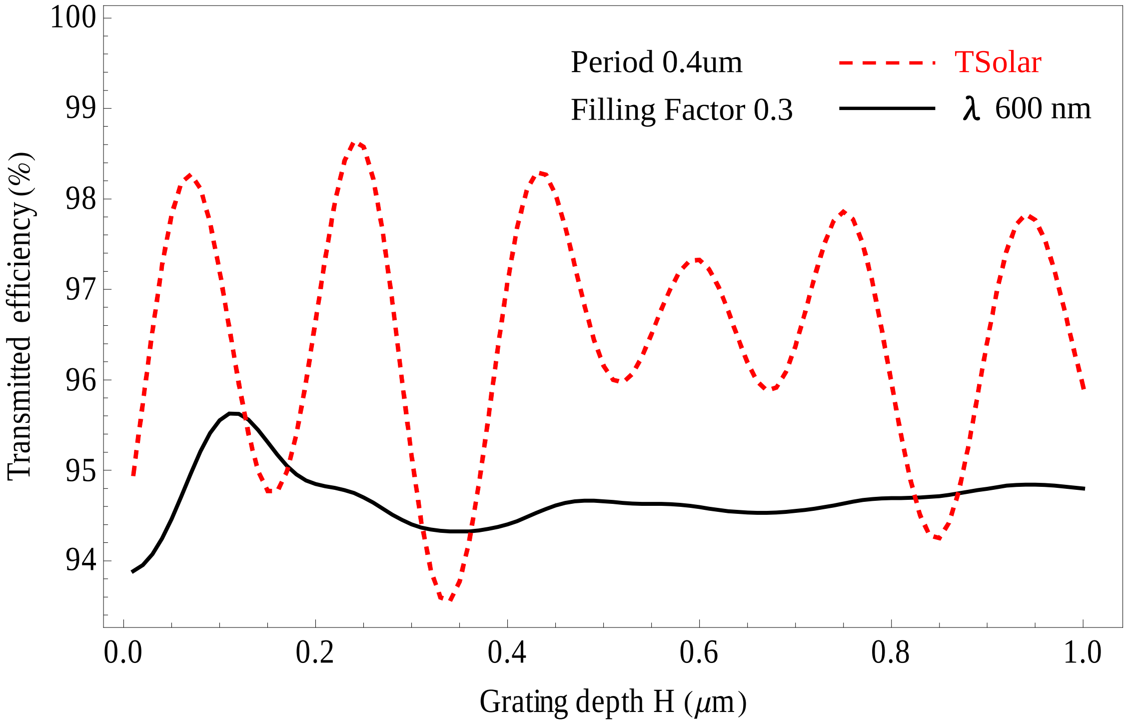

Figure 3.3 The transmittance comparison of TSolar to wavelength 600 nm as function of grating depth, with period 0.4 um, filling factor 0.3

According to (2.3) if a grating with its period less than half the wavelength of incident light, only lower diffracted order will present and other higher orders are evanescent. This kind of grating is called sub-wavelength grating, and shown to contain broadband properties [9]. From theoretical consideration, if we only consider certain wavelength, eg. $\lambda = 600\ \text{nm}$, the depth of the grating has to be 300 nm with period 400 nm and filling factor 0.3 in order to achieve higher transmittance over 98%. As for solar applications, it is more practical to value TSolar. Therefore the transmittance would be different when TSolar is taking into consideration. Figure 3.3 indicates the maximum transmitted efficiency is over 95% with the grating depth around 100 nm. Moreover, it is more feasible to produce a 100 nm depth grating than 300 nm.

### Optimum grating configuration

To find out the optimum height, period and width of grating, approximations were made based on assumptions consistent with theory [9]. Typical value shows out the depth of grating, H, in the scale of nanometer is possible lower, and therefore we firstly fix H at certain theoretical expected values, which begins at lower limit of 50nm, and change the other two variables, period and width, to extract optimum parameter. We then increase H step by step and compare every optimum value in each run. H was roughly estimated using plot of comparison in Table 3.1, which demonstrates the reflectivity contour map of TSolar as functions of period and filling factor.

By increasing H every 50 nm each plot, a low value of reflectivity of less than 5% can only be obtained with $0.05\,\mu\text{m} < \text{H} < 0.25\mu\text{m}$. Although the lowest peak of reflectivity shifts toward larger period and smaller filling factor with higher H, the fabrication process is relatively difficult and also the reflectivity are all over 5%. Additionally, a larger ratio of depth over period naturally results in a larger surface area, which increases the possibility of surface recombination in solar cells. In this aspect, it is inferred that with H $0.1\,\mu\text{m}$, period 0.3~0.4 and filling factor 0.3~0.4 is effective for reducing the surface reflection loss without severe surface recombination loss.

Table 3.1

Contour Map of reflectivity of different height of grating H as functions of period and filling factor under the standard solar spectrum

| H | |
|---|---|
| 0.05 μm | 0.1 μm |
| 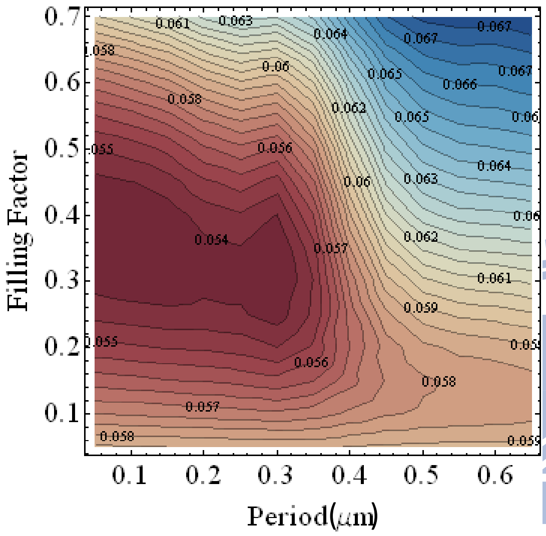 | 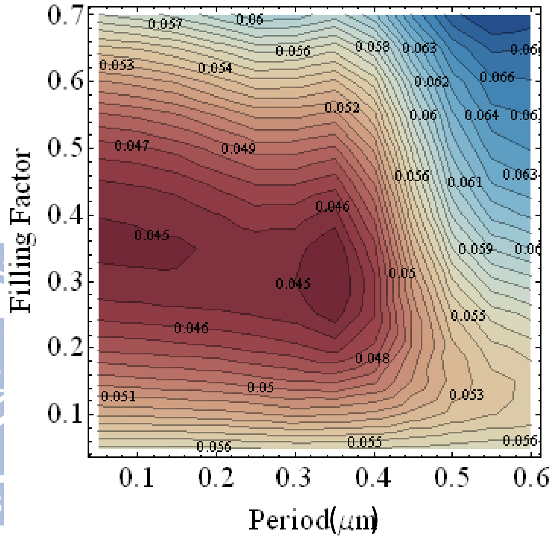 |
| 0.15um | 0.2um |
| 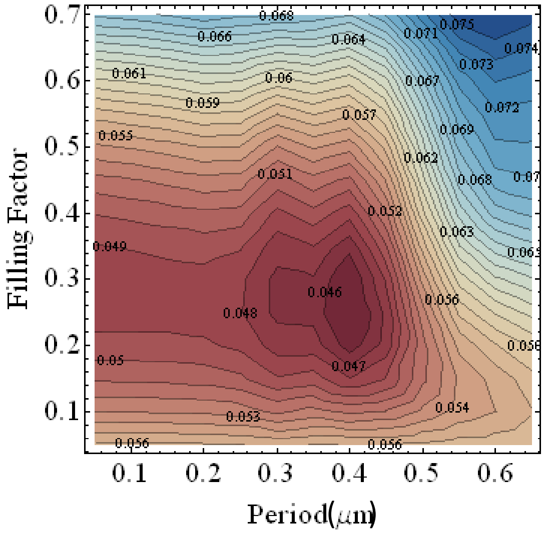 | 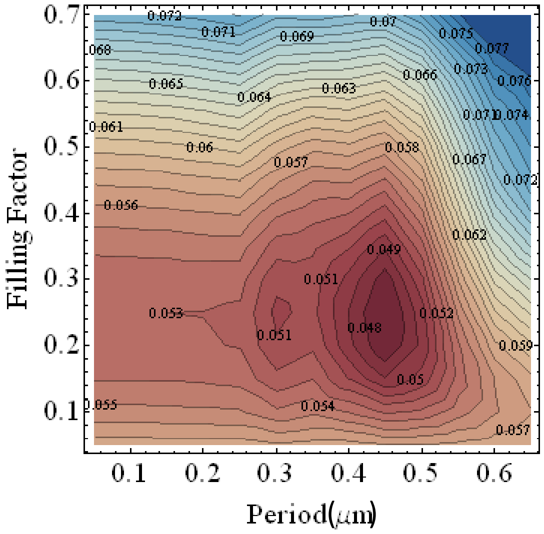 |

| 0.25μm | 0.3μm |
|---|---|
| 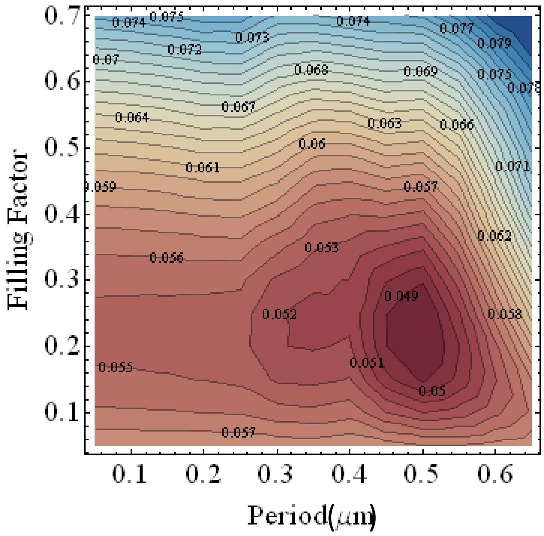 | 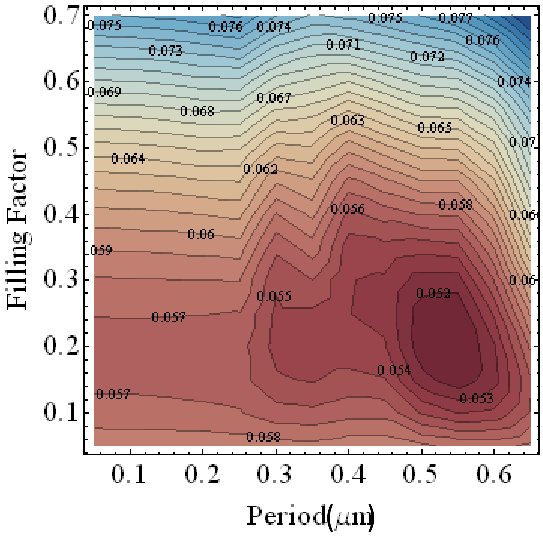 |
| 0.35μm | 0.4μm |
| 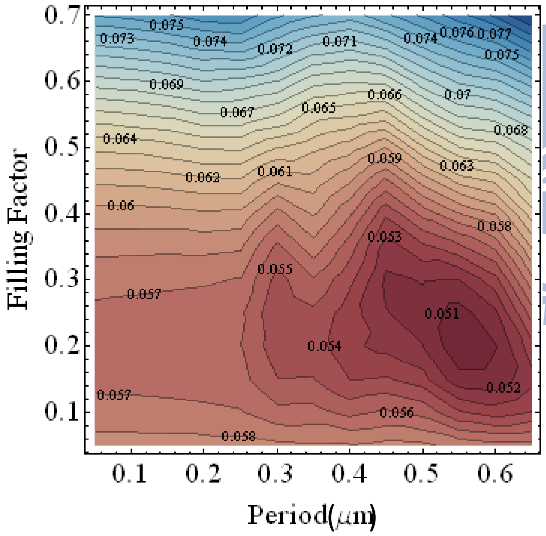 | 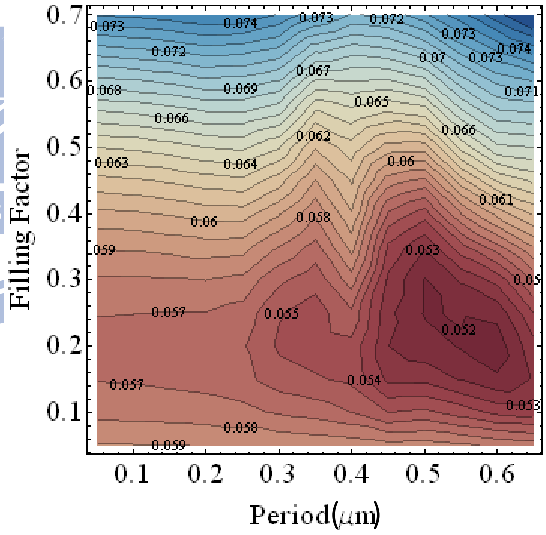 |

| 0.45um | 0.5um |
|---|---|
| 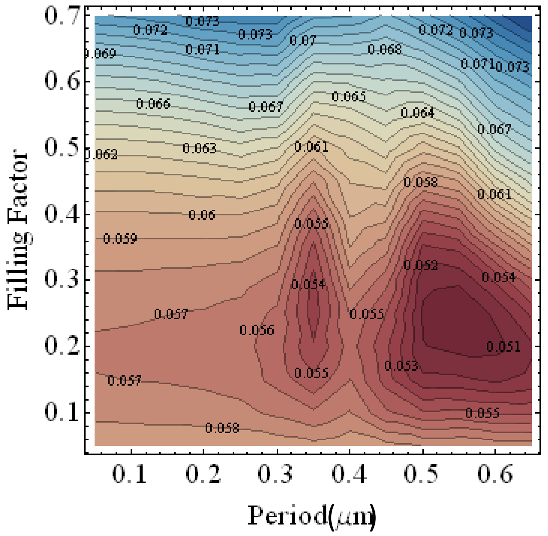 | 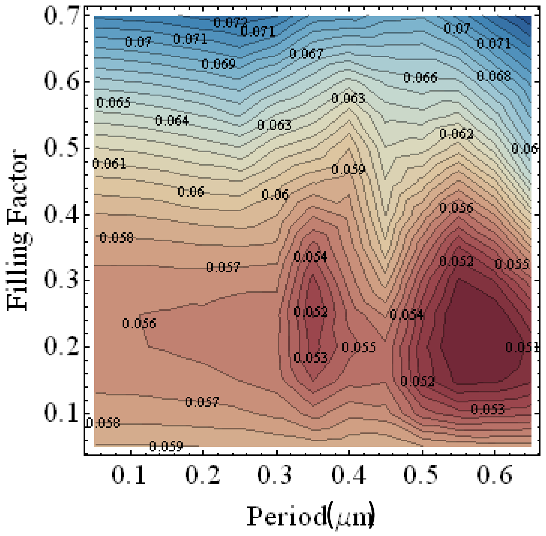 |

These values can be refined by iterative comparison, thus a preferable profile of grating is approximately chosen. We now fix the value of period to 0.35μm where indicated to have the lowest reflectivity in Table 1.1, and vary the depth and width of grating. The contour plot of transmittance at period 0.35μm as functions of grating depth and filling factor is shown in figure 3.4. The results turn out similar to previous estimation, that H around 0.1 μm and filling factor 0.3 marks the highest transmitted efficiency over 95%. It is noticeable that there is also another peak at higher depth and smaller filling factor exhibits to have transmitted efficiency over 94%. Unfortunately, due to the fabrication difficulties to produce a grating with depth 0.5μm 90° and width 60 nm, we should focus more attention on the feasible outcome on the left side of figure 3.4.

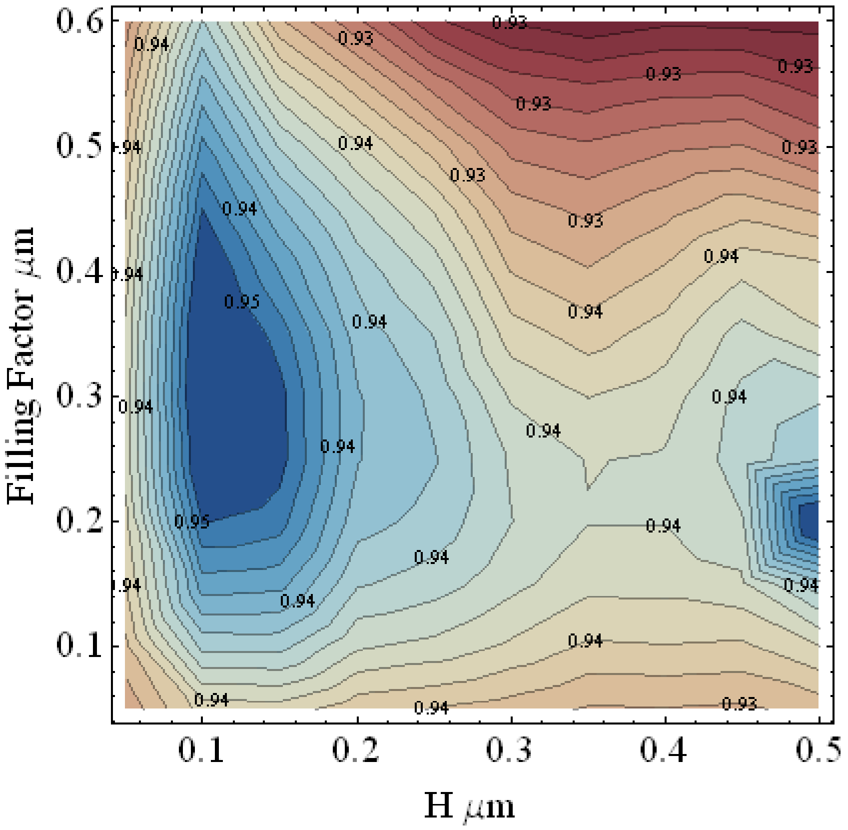

Figure 3.4 Contour map of transmittance under standard solar spectrum of grating period 0.35um as functions of height and FF

### Result of optimum grating structure

Consequently, the extraction of optimized filling factor and period had been determined. The results are shown in figure 3.5 below where the value of filling factor is 0.3 and period 0.35um which demonstrates the transmitted efficiency to be up to 95% at normal incidence. Finally, the optimum periodic 1D grating structure is then plotted in unit cell shown in figure 3.6.

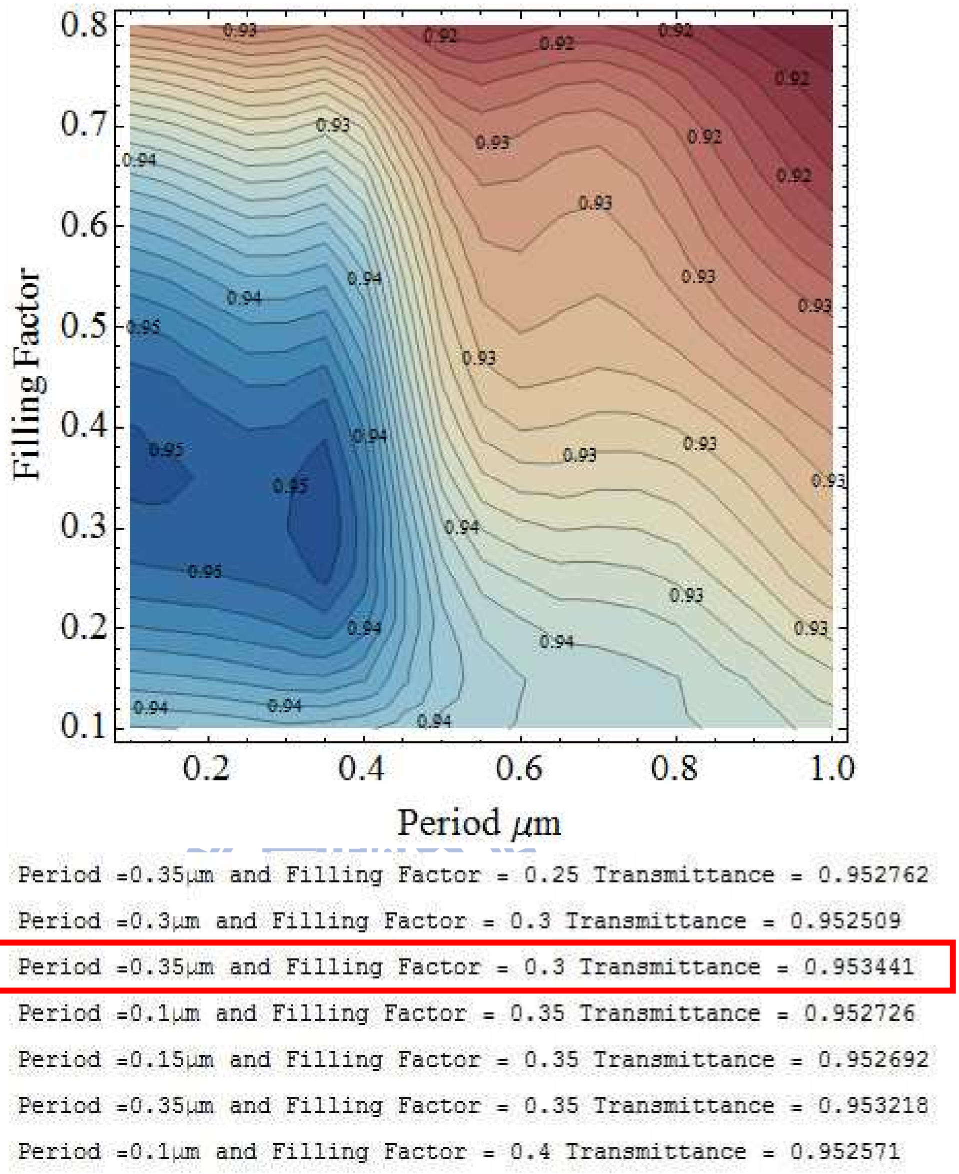

```
Period =0.35μm and Filling Factor = 0.25 Transmittance = 0.952762
Period =0.3μm and Filling Factor = 0.3 Transmittance = 0.952509
Period =0.35μm and Filling Factor = 0.3 Transmittance = 0.953441
Period =0.1μm and Filling Factor = 0.35 Transmittance = 0.952726
Period =0.15μm and Filling Factor = 0.35 Transmittance = 0.952692
Period =0.35μm and Filling Factor = 0.35 Transmittance = 0.953218
Period =0.1μm and Filling Factor = 0.4 Transmittance = 0.952571
```

Figure 3.5 The optimum value of grating profile

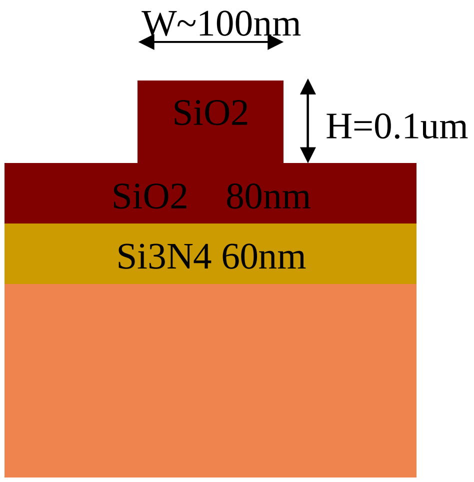

Figure 3.6 The unit cell of optimum periodic 1D grating profile

Figure 3.7 compares the transmittance of two surface conditions with and without grating structure at normal incidence. Although the transmittance rate of surface with grating is not always surpass throughout the whole wavelength, it is the TSolar that plays a crucial parts and dominates throughout the whole incident angle in figure 3.8.

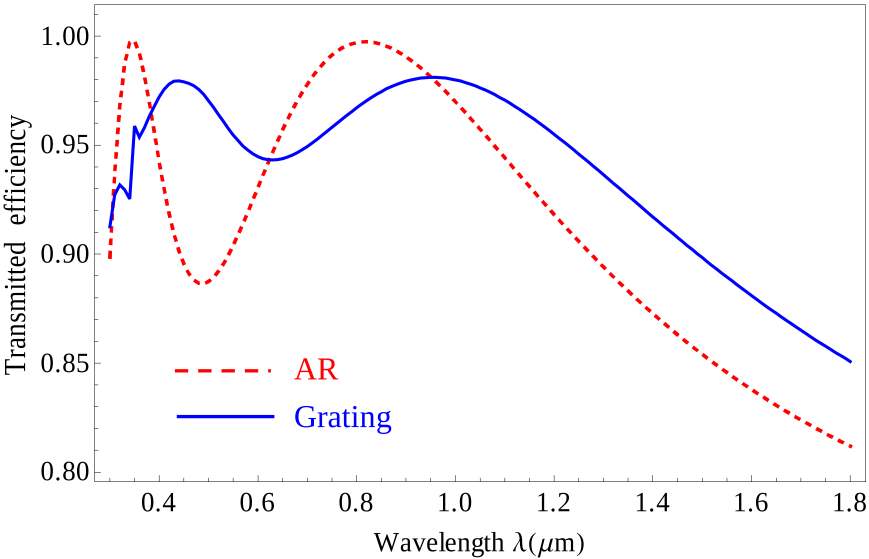

Figure 3.7 Transmittance comparison of sample with AR and grating as function of wavelength

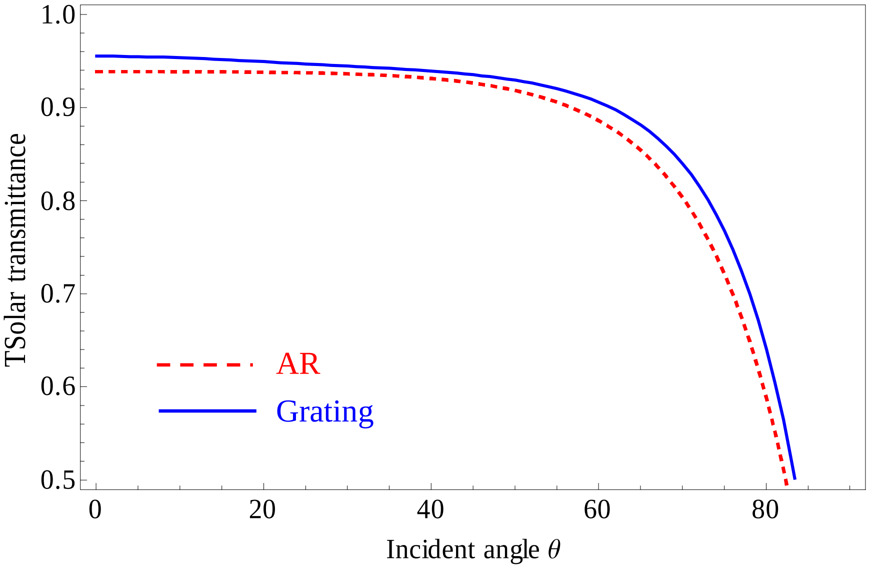

Figure 3.8 TSolar comparison of AR and Grating cell as function of incident angle

## 3.3 Broadband Characteristic at Oblique incidence

As expected the broadband absorption at oblique incidence, figure 3.9 shows the subtraction between two curves in figure 3.8. It indicates the enhancement effect is stronger (> 5%) at higher incident angle. This improvement can be contributed to the geometric form of grating. Figure 3.10 shows the distribution of TE and TM polarization to TSolar throughout whole incident angle. TE modes decade faster than TM at higher incidence, while TM modes compensate the reflection loss caused by TE polarization.

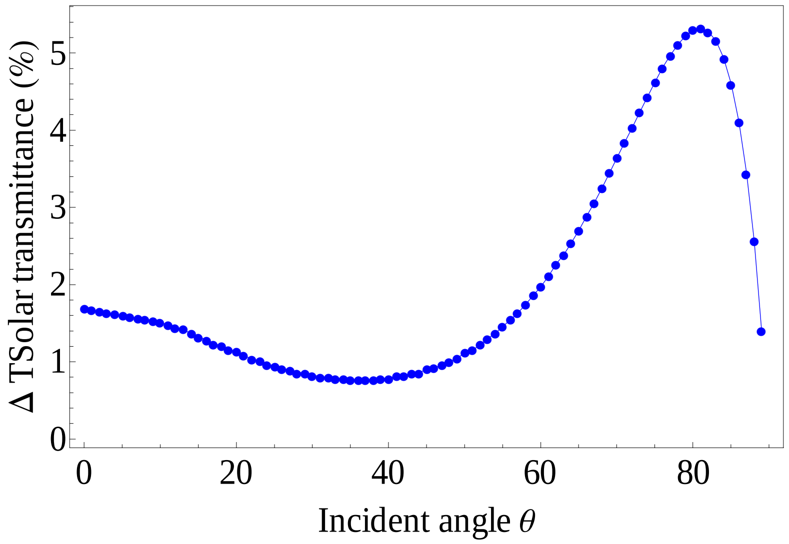

Figure 3.9 The TSoalr difference between sample with and without grating

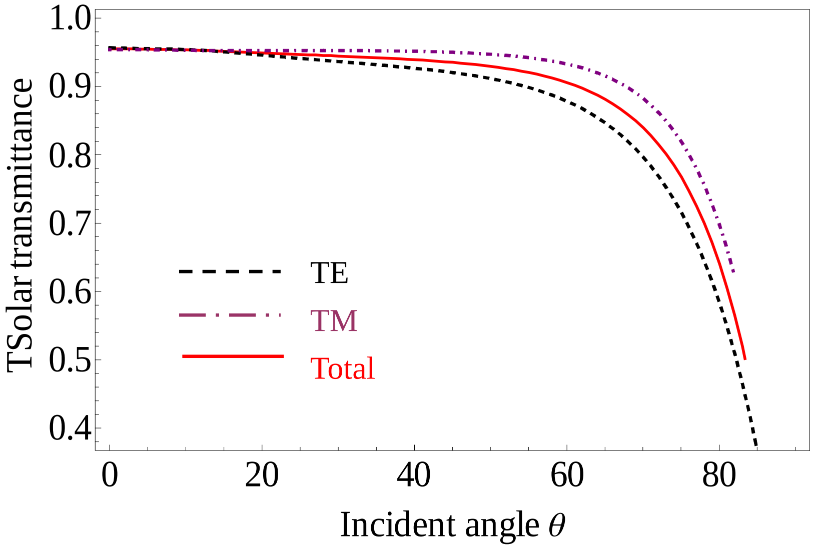

Figure 3.10 The contribution of TE & TM modes to TSolar as function of incident angle

### Wavelength distribution at different incident angle

Figure 3.11.a and 3.11.b shows the transmittance distribution of each wavelength at various incident angles with AR on the surface and AR with grating on the surface, respectively.

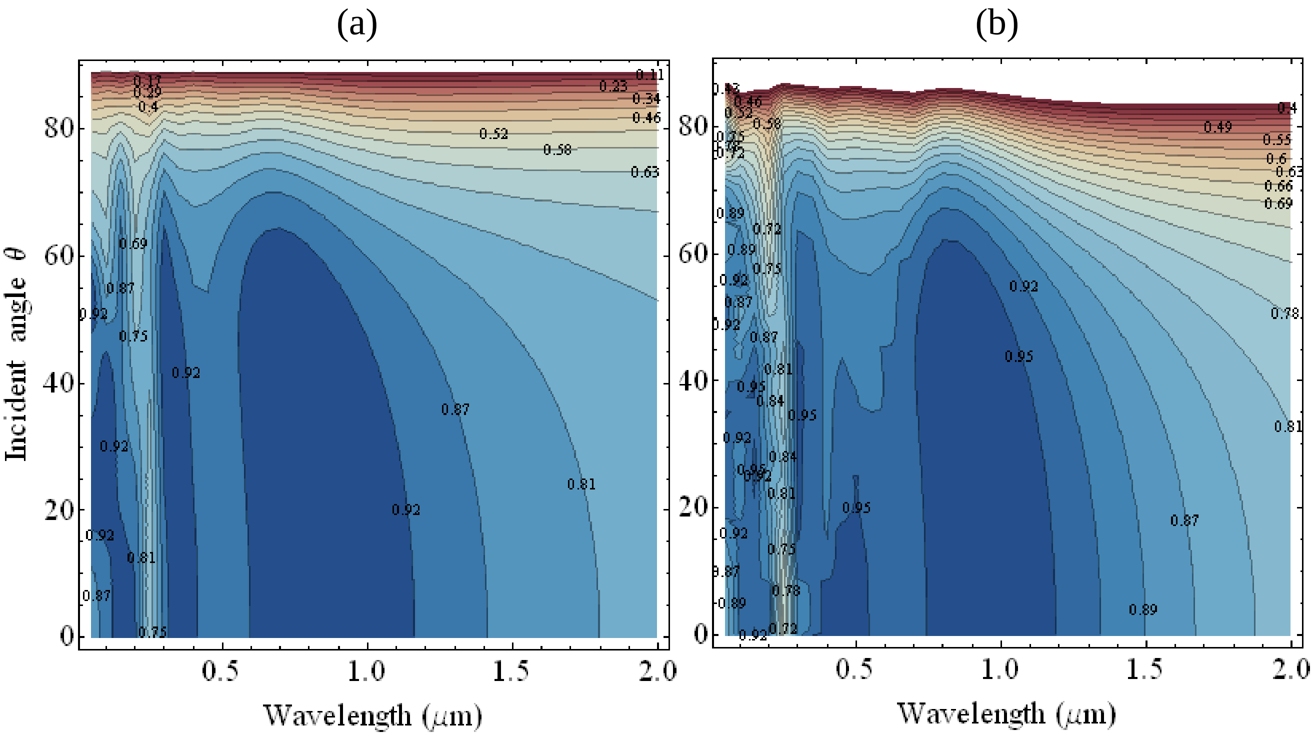

Figure 3.11 Contour map of transmittance of (a) AR and (b) AR with grating structure on the surface as functions of wavelength and incident angle

At the span of short wavelength, the transmittance in figure 3.11 (b) has better performance over 6% until 60 degree incident comparing to figure 3.11 (a). Throughout the middle span of wavelength between 0.6 μm to 1.2 μm, (b) can still suppress more than 2% at oblique incident.. It is also obvious to mention that transmittance raises invigorately more than 20%.. at larger incident angle. We then expect the increasing amount of light will successfully form electron-hole pairs and contribute to the improvements of photovoltaic energy conversion efficiencies.

As expected for sub-wavelength grating where only lower transmission order exist, figure 3.12 displays the TSolar transmitted distributions for different diffractive order of both TE and TM polarization, as function of incident angle. The light is almost diffracted into zero order, as well as at higher incidence, with only a partial portion of light parcel into first order.

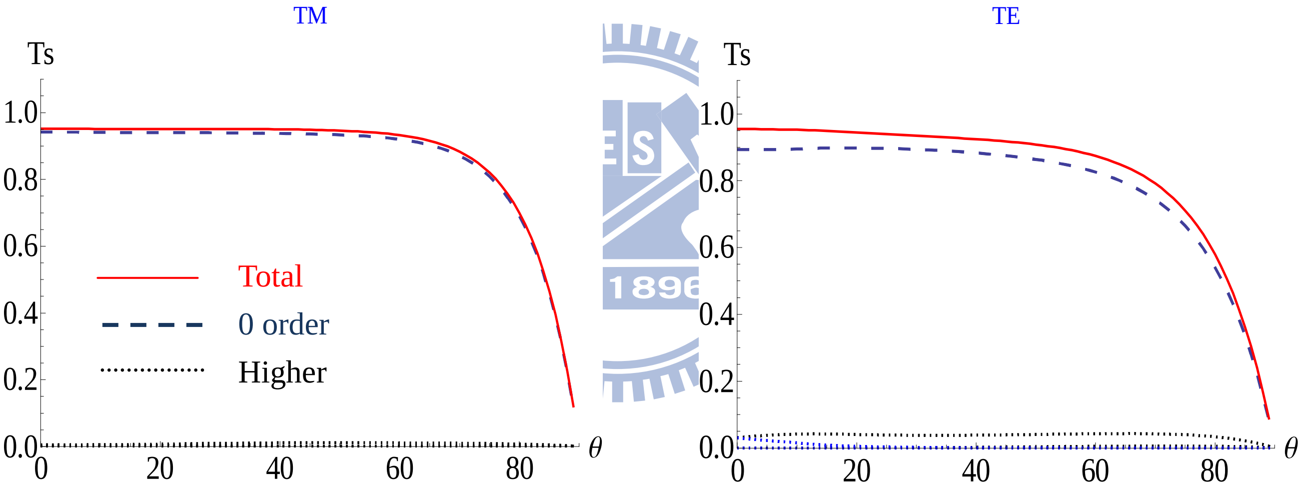

Figure 3.12 Displays of the transmittance diffractive order distributions as function of incident angle in TM(left) and TM(right) polarization

# Chapter 4

# Experimental Analysis and Discussion

## 4.1 Sample Design and Fabrication Process

The sample used here is InGaP/InGaAs/Ge triple junction solar cell provided by Visual Photonics Epitaxy Co. (VPEC). The structure is schematically shown in figure 4.1.

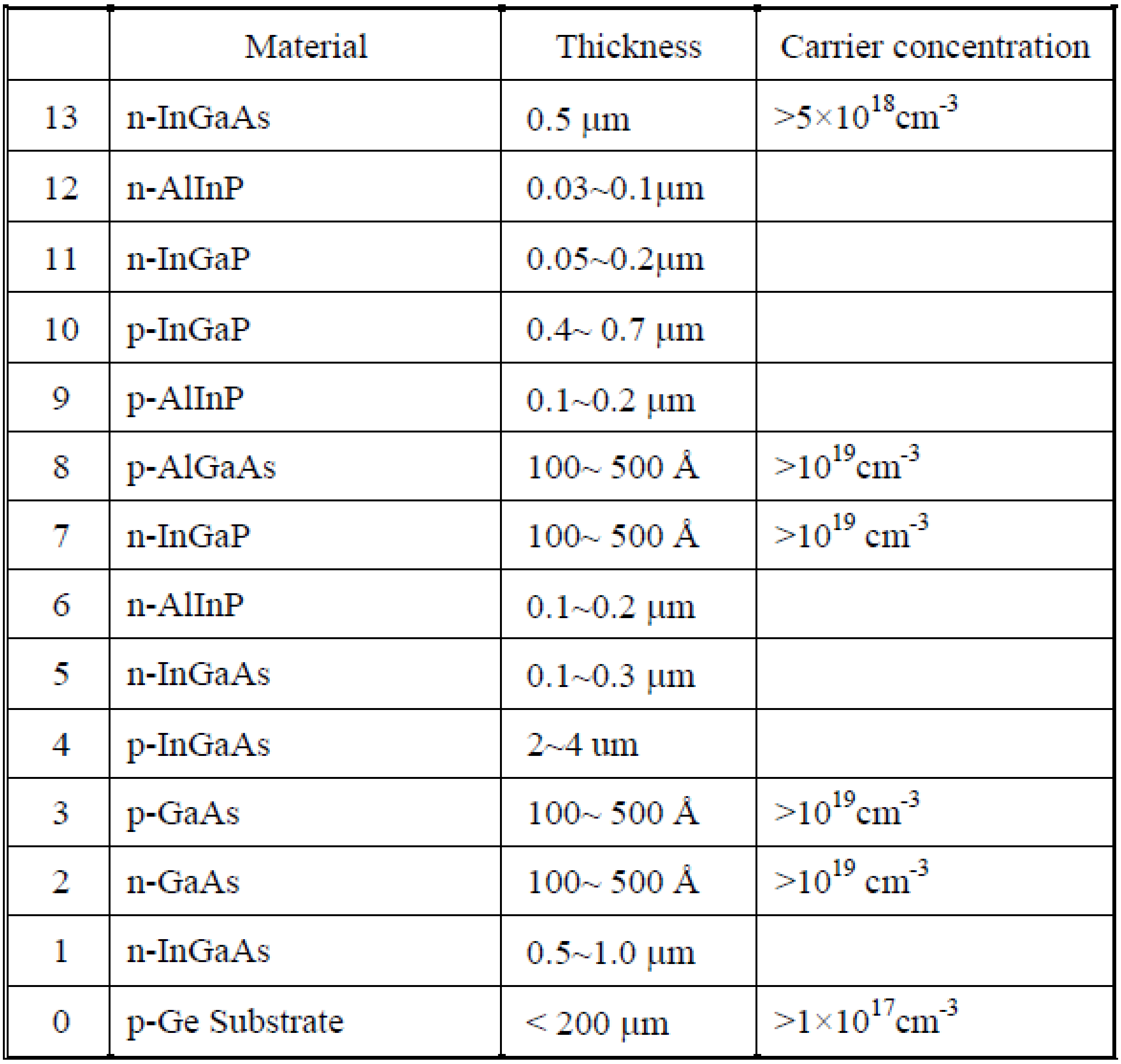

| | Material | Thickness | Carrier concentration |
|---|---|---|---|
| 13 | n-InGaAs | 0.5 μm | $>5\times10^{18}$cm$^{-3}$ |
| 12 | n-AlInP | 0.03~0.1μm | |
| 11 | n-InGaP | 0.05~0.2μm | |
| 10 | p-InGaP | 0.4~ 0.7 μm | |
| 9 | p-AlInP | 0.1~0.2 μm | |
| 8 | p-AlGaAs | 100~ 500 Å | $>10^{19}$cm$^{-3}$ |
| 7 | n-InGaP | 100~ 500 Å | $>10^{19}$ cm$^{-3}$ |
| 6 | n-AlInP | 0.1~0.2 μm | |
| 5 | n-InGaAs | 0.1~0.3 μm | |
| 4 | p-InGaAs | 2~4 um | |
| 3 | p-GaAs | 100~ 500 Å | $>10^{19}$cm$^{-3}$ |
| 2 | n-GaAs | 100~ 500 Å | $>10^{19}$ cm$^{-3}$ |
| 1 | n-InGaAs | 0.5~1.0 μm | |
| 0 | p-Ge Substrate | < 200 μm | $>1\times10^{17}$cm$^{-3}$ |

Figure 4.1 Structure of triple junction concentration solar cell

In order to compare the effect of grating structure after realizing it onto surface of solar cell, three kinds of device will be made, including device without AR coating, with AR coating and with grating on top after AR coating. The standard process for these three kinds includes:

(1) Step 1: Photo lithography for electrode pattern. (figure 4.2)

To reduce the series resistance between grid electrode, it is evaluated by using equivalent circuit model in figure 1.9 and calculate by certain simulation program [27,28]. Therefore, the suitable configuration of electrode contact can be designed with grid width 5 $\mu m$ and pitch 112 $\mu m$ inside 1mm square and the total shadow loss due to contact coverage is about 5%. Moreover the ohmic contact resistance can sufficiently be reduced by depositing Ni/Ge/Au alloy onto highly doping $N^+$-InGaAs layer and Ti/Au alloy on $P^+$-Ge substrate. After evaporating electrodes, the device then put to annealing at 400°C for 30 seconds. It is requisite to etch off the $N^+$ capping layer with certain kinds of acid solvents [29] and to expose AlInP window layer before depositing AR coating. The acid solution used here is $H_2SO_4$, $H_2O_2$, $H_2O$ (1:8:80).

The device without AR is done and shown in figure 4.3. We then proceed to the second kind of device where AR coating is deposited on top of surface.

(2) Step 2: Anti-reflection coating. (figure 4.4)

Two flat dielectric AR coating layers, $Si_3N_4$ and $SiO_2$, are deposited, at the optimized thickness, 60nm and 80nm respectively by using PECVD technique. By using BOE solvent, the electrode covered by AR can be revealed. Be sure to make the soaking time inside BOE as precise as possible, thus lowering the risk of any chance for lateral penetration which might damage the wafer.

The second kind of device is done and shown in figure 4.5. Lastly, we will continue to put the grating structure onto AR layer. The fabrication of grating structure in the scale of nanometer can not be completed using photo-lithography. Consequently, E-beam lithography technique is introduced to pattern the period structure.

(3) Step 3: E-beam lithography for sub-wavelength grating. (figure 4.6)

As a result of the optimization in chapter 3, the period and width of the grating are designed to be 350nm and 100nm respectively. PMMA is a high contrast positive resist and has good adhesion on nearly any surface, thus has been widely applied for nano-lithography. During the process, it is better to create an undercut profile on resist, thus making it easier to life-off. To perform such undercut profile, it requires two layers of PMMA with different solvent concentration, A3 and A5. Due to the different dissolution properties from each layer, undercut can be made as controlling the developing time carefully by means of develop solvent MIBK (figure 4.6.1). Afterwards the 100 nm thicknesses of $SiO_2$ gratings are thermally evaporated using E-gun (figure 4.6.2), and lift-off process can be easily done when soaking in acetone without further agitation (figure 4.6.3).

Figure 4.7 shows the top view of SEM image. We also obtain different width from 100nm to 150nm. Therefore, further investigations of the effect caused by various width of grating can also be discussed in the following section.

## Step 1 Photolithography for electrode

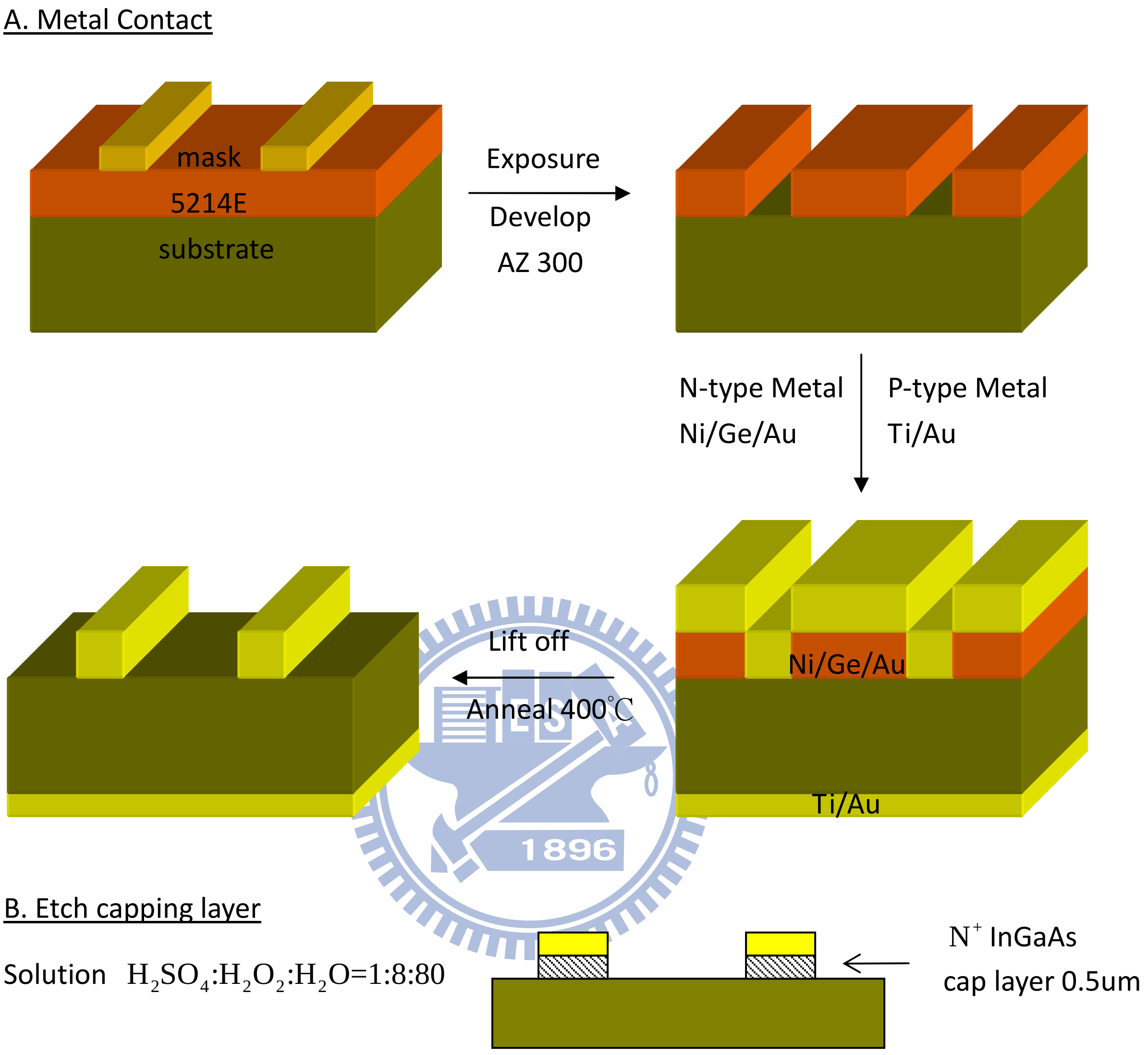

Figure 4.2 Photo lithography process for electrode pattern

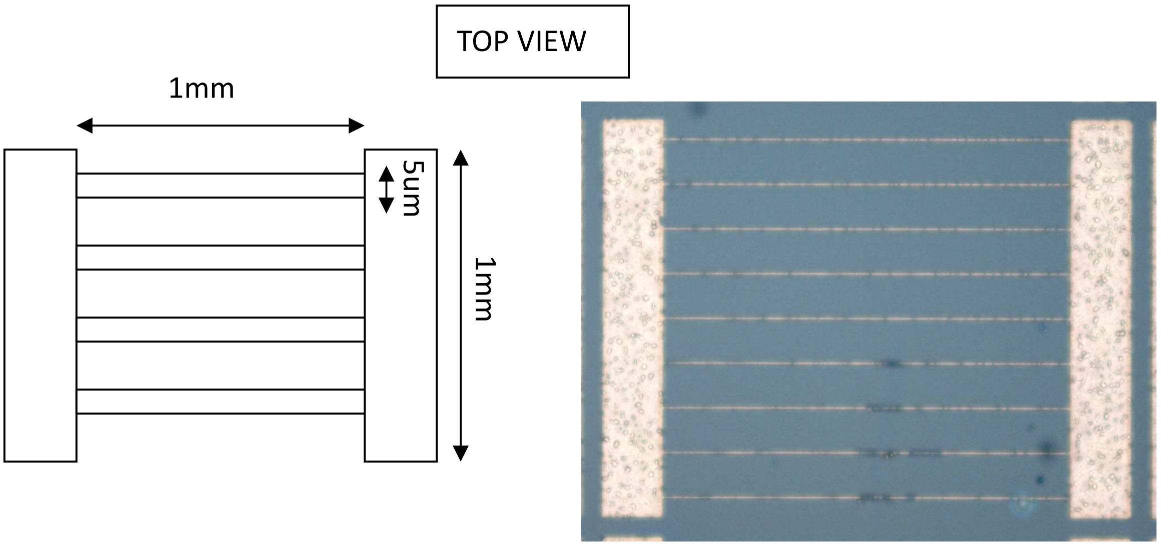

Figure 4.3 Electrode contact configuration

STEP 2 AR Coating

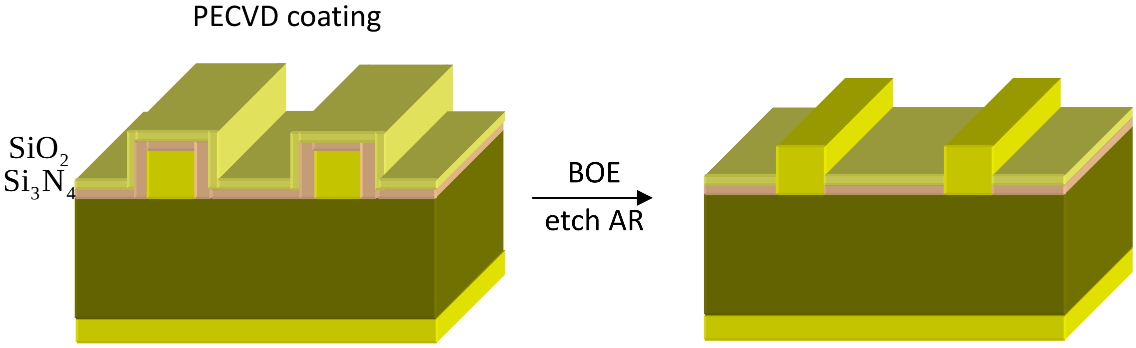

Figure 4.4 Anti-reflection coating process

Top view

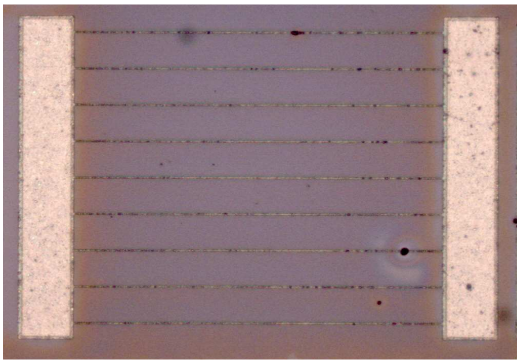

Figure 4.5 Electrode contact configuration after removing AR by using acid BOE

## Step 3 E Beam Lithography

A. Grating pattern set

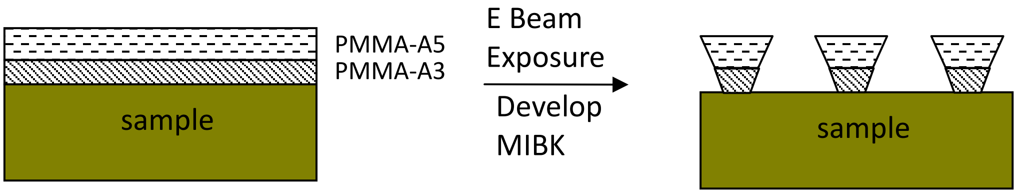

B. E-Gun $SiO_2$ Coating

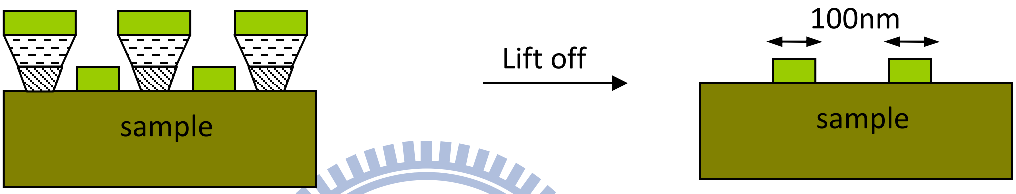

After E-beam exposure

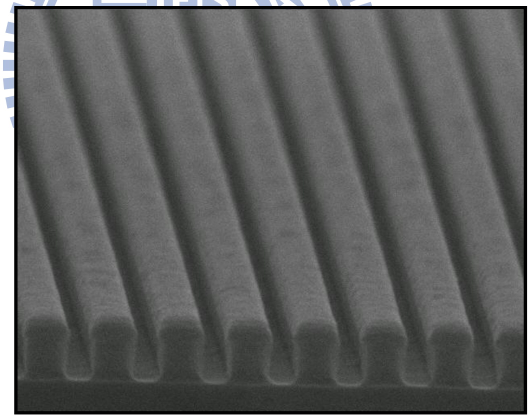

Figure 4.6.1

Deposit $SiO_2$

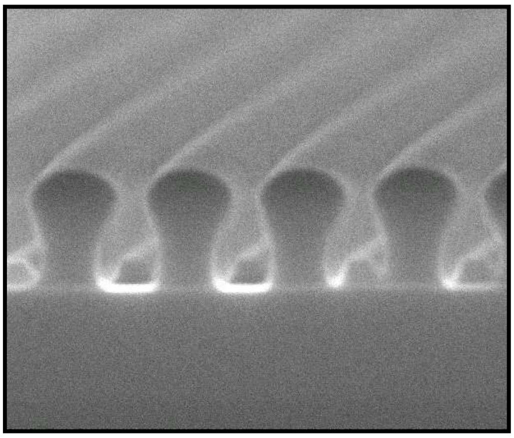

After lift off

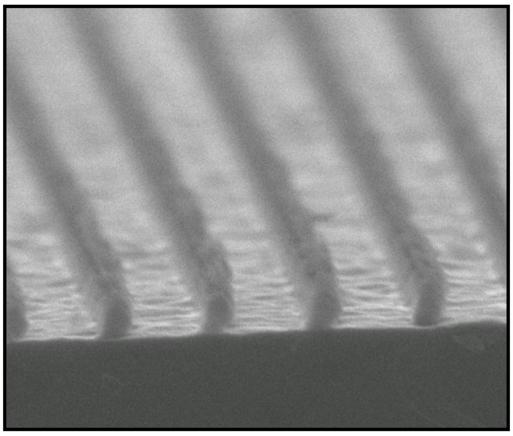

Figure 4.6.2

Figure 4.6.3

Figure 4.6 E-Beam lithography process for sub-wavelength grating

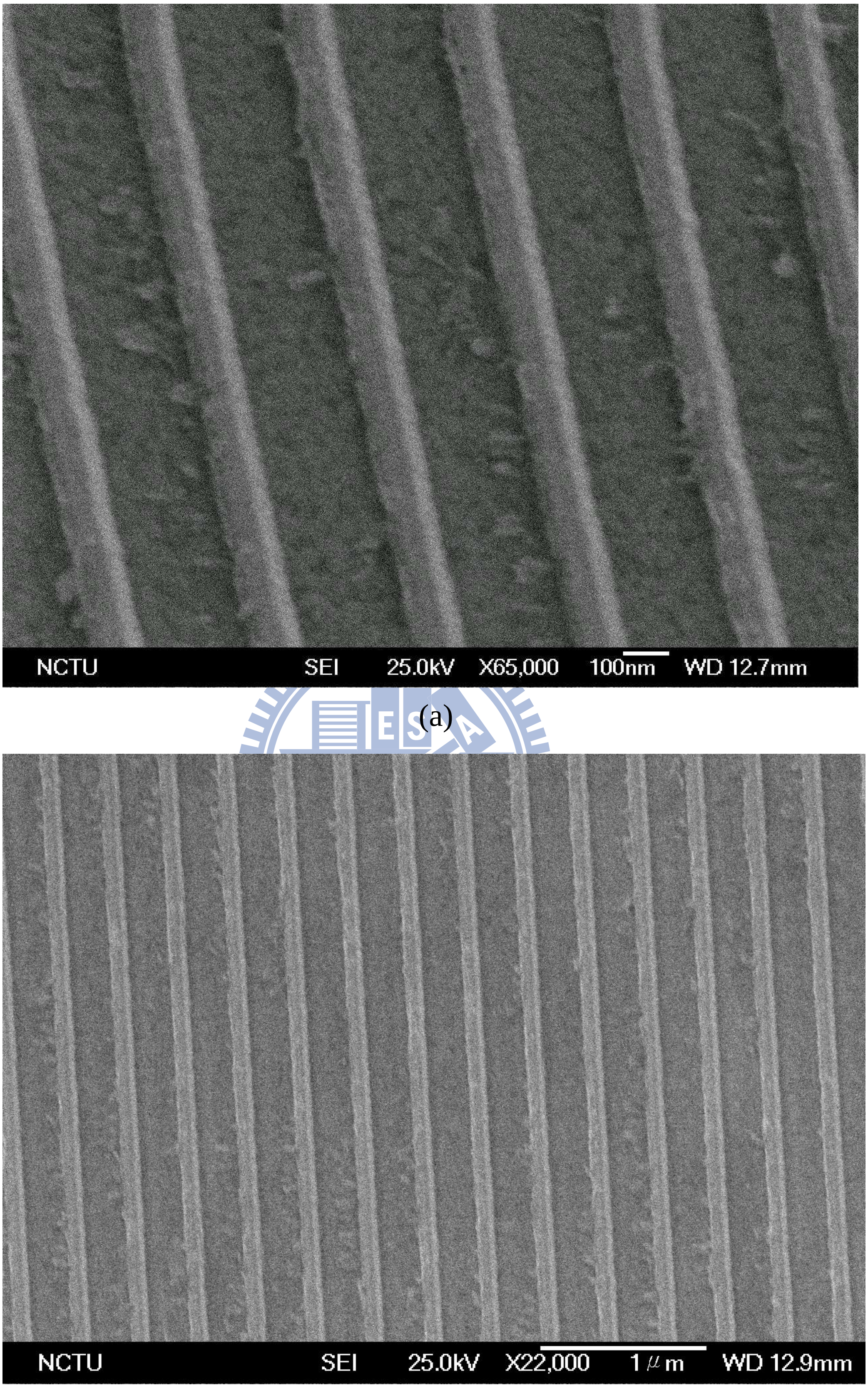

(a)

(b)

Figure 4.7 Top view of SEM image of grating with period 350nm, depth100nm and width 100nm under (a) large scale (b) small scale

## 4.2 Measurement and Analysis

### Instrument

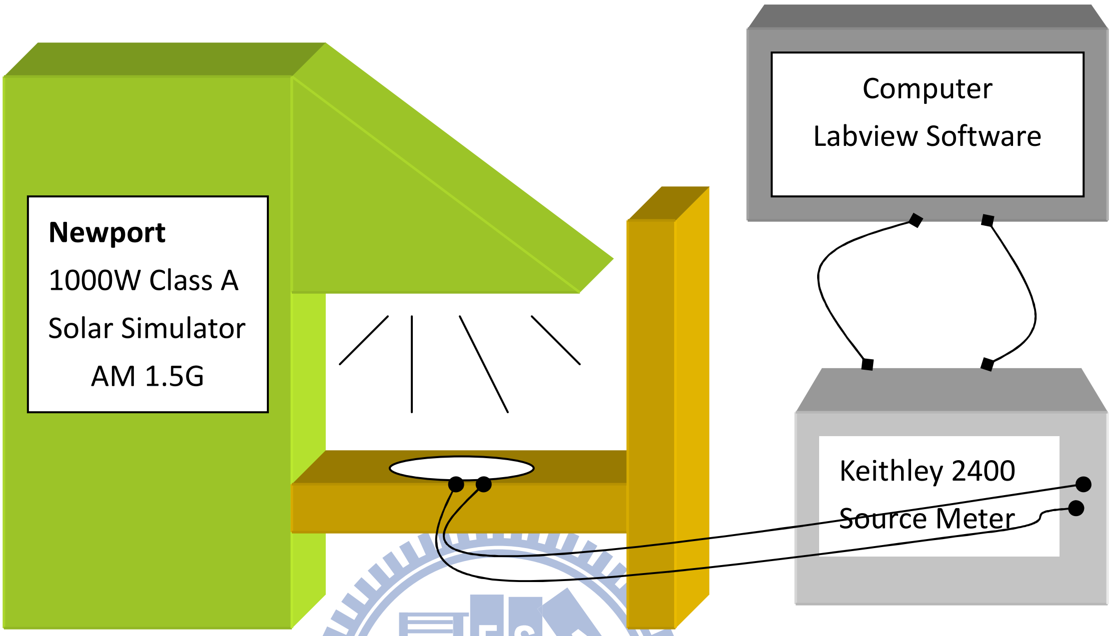

Figure 4.8 Solar simulator system diagram

The measurements are done by a set of Newport AM1.5G 1000W solar simulators (figure 4.8) in Prof. Peichen Yu's Lab in the department of Photonics at NCTU. It is certified according to ASTM 927-05 standards by using xenon lamp to match Class A performance and calibrated by standard tested solar cell before each measurement. The current-voltage data are taken by Keithley 2400 source meter, which is controlled by the Labview software to extract the data and parameters. To test the solar efficiency under various incident angles, a uni-axial rotation stage is set up where the sample is attached onto the stage. We regulate the rotation state by testing the maximum efficiency as normal incidence.

## Current-voltage characteristic

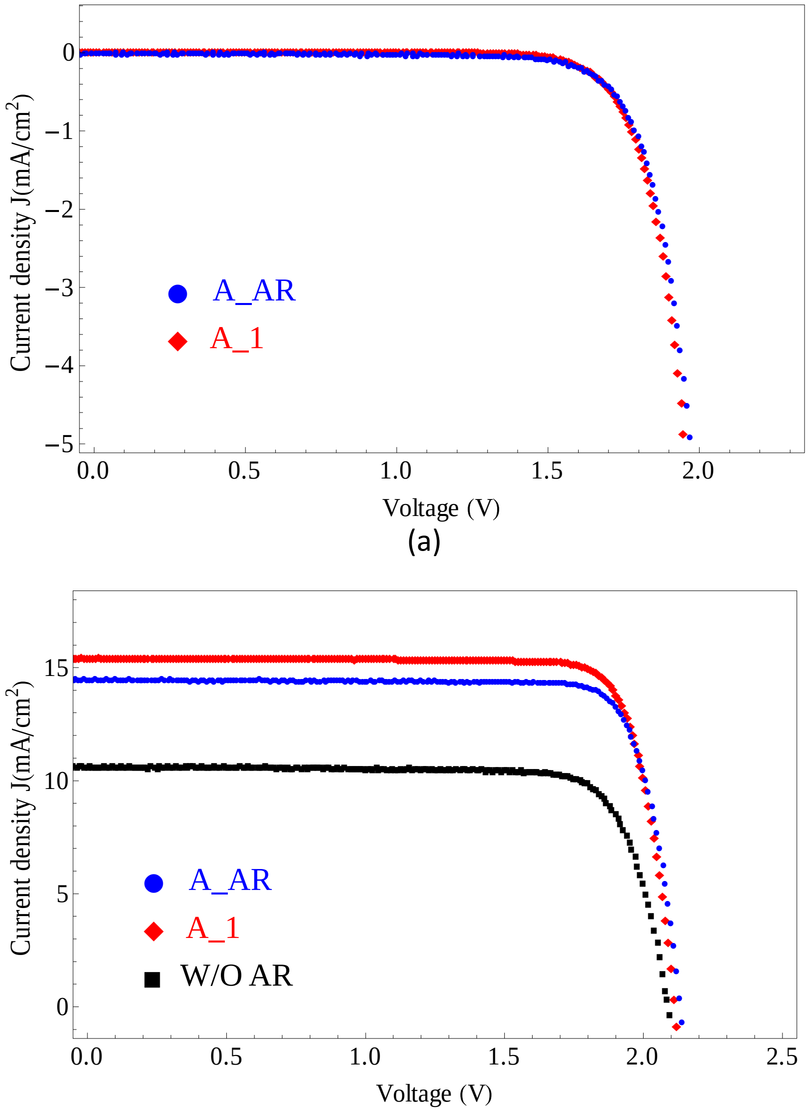

(a)

(b)

Figure 4.9 J-V curves of (a) dark current with sample A_AR and A_1t
(b) under illumination with sample A_AR, A_1 and W/O AR.

Figure 4.9 (a) shows the dark current-voltage curve of sample A_AR of AR without grating structure on top, and sample A_1 with grating of period 0.35 μm, width 105nm and depth 100nm. The measurements of these two samples match quite the same. Some electrical properties can be approximately derived from dark current-voltage of characteristics which provides essential information of performance loss and device efficiency. But this numerical analysis is beyond the scope of our discussion [30,31]. However, we can still assume the insight electrical properties to be similar by looking at the tendency of dark current-voltage to make sure there will not be too many uncertainties to affect the experimental outcome. Figure 4.9 (b) presents the current-voltage curve of sample under illumination. Here we also compare the sample W/O_AR , without AR coating on the surface, thus to observe the effect of AR and grating mechanism. It shows A_1 has higher short current density, comparing with the other samples.

As we know, the net absorbed photon flux from the sum results in the photocurrent, therefore the short circuit density can be briefly represented as integrating the amount of circuit density over photon energies:

$$J_{sh} = q\int_{E_g}^{\infty} \eta(E)(1-R(E))P(E)I(E,T)dE \tag{4.1}$$

$P(E)$ is the probability of absorption of a photon of energy E, $R(E)$ is the probability of photon being reflected on the surface and q is the electronic charge. Each electron has the probability, $\eta(E)$, of being transferred to the external circuit. $I(E,T)$ refers to the photon flux emitted normal to the surface at energy E of a black body radiation at temperature T. With the definition of quantum efficiency, $QE(E)$, defined as the chance of an incident photon of energy E will deliver one electron to the external circuit, (4.1) can be rewritten as:

$$J_{sh} = q\int_{E_g}^{\infty} QE(E)I(E,T)dE \tag{4.2}$$

Consequently, we may attribute the enhancement to grating structure which yields more light to couple inside solar cell, which reduce the reflection in (4.1) and increase the quantum efficiency in (4.2). On the other hand, the longer optical path due to diffracted light which improves the minority carrier lifetimes may also take into accounts.

Moreover, as we know the MJ solar cell has different current density among each cell, which means the current matching analysis is quite a crucial technique for enhancing short circuit current. Simulation for this current matching issue has long been studied [3,4]. Figure 4.10 shows a simulation I-V curve done by APSYS commercial software which performs with front AR layers $MgF_2/ZnS$. It should be mentioned that due to current mismatching, short current density is about 16 $A/m^2$ and much of the current component is wasted in the middle subcell. The open voltage is the sum up voltage of each subcell around 2.6 V. In our case of study, all the cell performances are lower than expected. As long as the dark current-voltage tendency shows no obvious division, it will not affect the experimental results by comparison. And further discussion about this will be mentioned later.

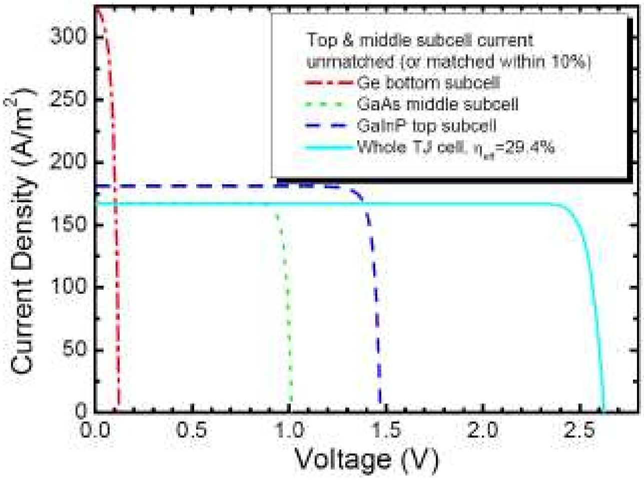

Figure 4.10 Simulation I-V curve of III-V solar cell done by APSYS commercial software which assumes front ARC layers to be $MgF_2/ZnS$

### Enhancement of short circuit current at oblique incidence

| Sample | Width | FF % | Jsh ($mA/m^2$) | Voc (V) | QE (%) |
|---|---|---|---|---|---|
| NOAR | | | | | |
| NAR | | 82.33 | 12.02 | 2.05 | 20.21 |
| A | | | | | |
| A_1 | 105nm | 83.07 | 15.04 | 2.12 | 26.50 |
| A_AR | | 83.09 | 14.50 | 2.13 | 25.72 |
| B | | | | | |
| B_1 | 105nm | 83.18 | 13.34 | 2.10 | 23.63 |
| B_2 | 140nm | 81.93 | 13.12 | 2.10 | 22.41 |
| B_AR | | 81.15 | 13.28 | 2.12 | 22.95 |
| C | | | | | |
| C_1 | 100nm | 80.48 | 14.75 | 2.08 | 24.48 |
| C_2 | 150nm | 83.55 | 12.26 | 2.09 | 21.23 |
| C_AR | | 81.47 | 13.36 | 2.11 | 22.59 |

Table 4.1 Experimental parameter of samples measured in different run

Table 4.1 is a list of experimental results of devices produced in different run of fabrication process; A, B, C. To avoid the deviation occurring in each run, it is better to compare the effect of grating and different performances by using the devices in the same process. The width of grating is confirmed by SEM and recorded in Table 4.1 in order to prevent any inaccuracy aroused by E-Beam lithography.

Equation (4.2) shows that short circuit current density is related to total amount of photon absorbed and delivered to the external circuit. Therefore, by measuring the external quantum efficiency, EQE, over wavelength, $J_{sh}$ can be roughly estimated. Figure 4.11 presents the EQE for each subcell. Obviously, we notice MJ solar cell can fairly transfer photon into electron over broadband from $0.3\mu m$ to $1.8\mu m$.

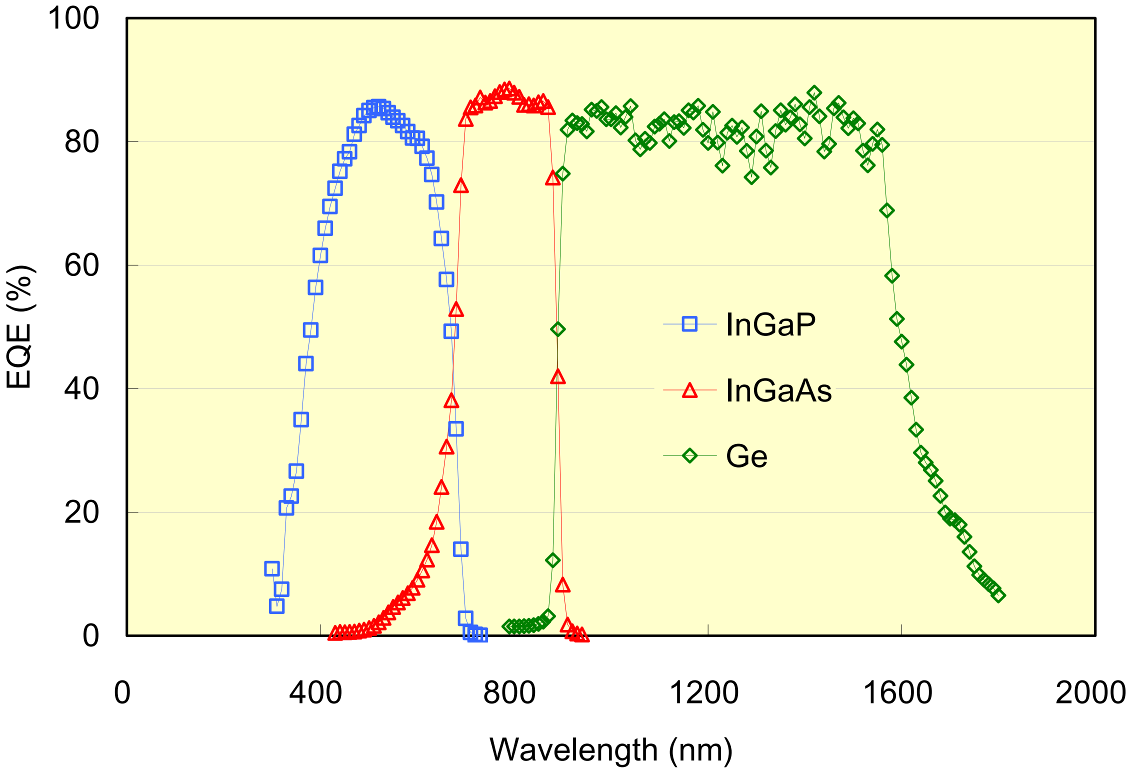

Figure 4.11 External quantum efficiency, EQE, of each subcell

Grating mechanism has been estimated to have better transmittance, which also means to enhance the total amount of photon pass inside the surface. As a result, the proportion of current density between sample with AR coating, $J_{sh,AR}$, and after manufacturing the grating structure, $J_{sh,G}$, over incident angle from normal to parallel is equivalence to ratio of the amount of photon effectively utilized by surface with AR, $N_{ph,AR}$, and grating, $N_{ph,G}$, respectively.

$$\frac{J_{sh,G}}{J_{sh,AR}} = \frac{q\int \Delta T(E)QE(E)I(E)dE}{q\int QE(E)I(E)dE} = \frac{N_{ph,G}}{N_{ph,AR}} \tag{4.3}$$

$\Delta T$ is the portion of increasing transmittance at energy E. Figure 4.12 shows the experimental results of $J_{sh,G}/J_{sh,AR}$ over incident angle. Comparing the ratio of total amount of photon, $N_{ph,G} / N_{ph,AR}$, calculated theoretically by means of figure 4.11, figure 4.13 displays the forward tendency throughout the whole incidence and an evident step up over 50 degree of incidence.

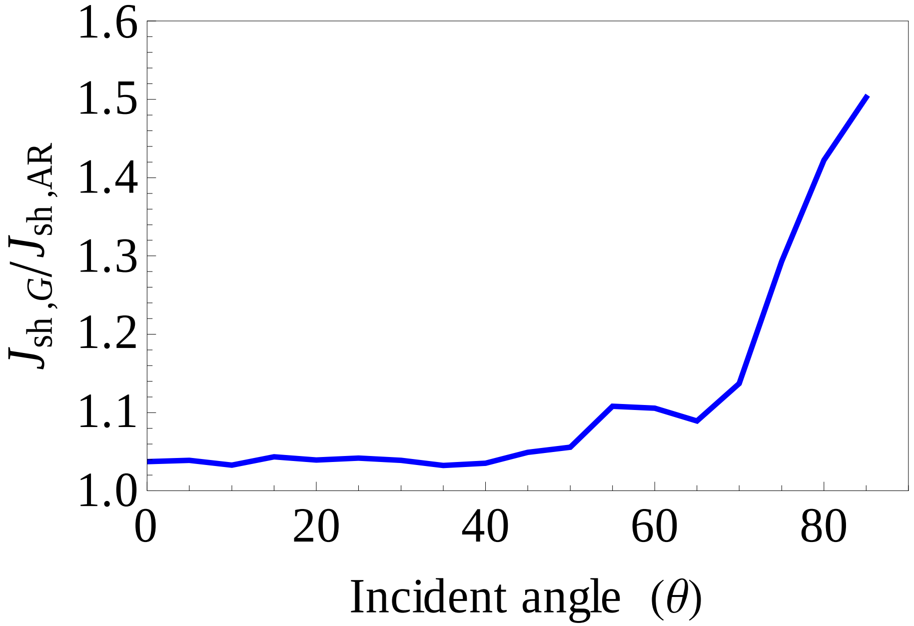

Figure 4.12 Ratio of short circuit current density between sample A_1 and A_AR over incident angle

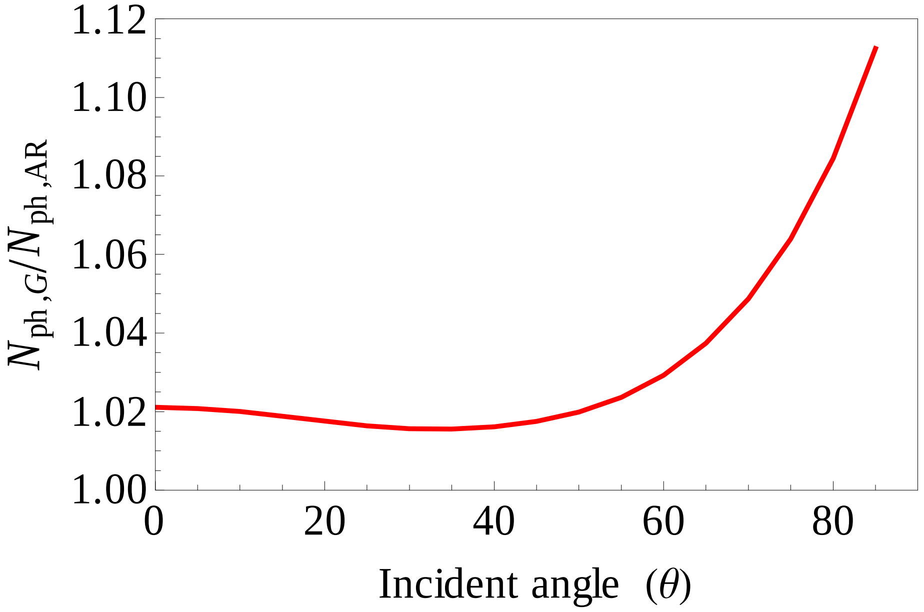

Figure 4.13 Ratio of number of photons utilized by surface of grating over AR coating.

### Enhancement of efficiency at oblique incidence

Generally, the maximum power density delivered is forward relation to short circuit current that we had discussed in previous section, which may also response on the conversing efficiency. According to table 4.1, the efficiency gets higher for the cell with grating on the surface than those without. In the theoretical point of view, the enhancement of photon collection of grating is justified by sample A_1, B_1 and C_1 with the grating width more or less around 100nm. We then want to investigate the changing of efficiency against oblique incidence. Due to the power density is dependence of incident angles; it should be dealt with as a factor over cosine of incident angle. To make it clearer to observe the effect, we compare the self-decay ratio of each cell, which is defined as efficiency at oblique incidence divided at normal incidence.

$$\text{Decay Ratio}=\frac{QE(\theta)}{QE(0)}$$

As it is shown in figure 4.14, A_AR decays more rapidly at larger incidence. The difference between A_AR and A_1 as function of incident angel can also be obtained by the subtraction of efficiency such as to infer the enhancement caused by grating mechanism (figure 4.15). Apparently, they all remain slightness positive increment until 50 degree where it begins to present a distinct step up. This tendency is similar to the calculation about the TSolar transmittance subtraction in figure 3.9 which indicates the slower loss transmitted photons between surface with and without grating.

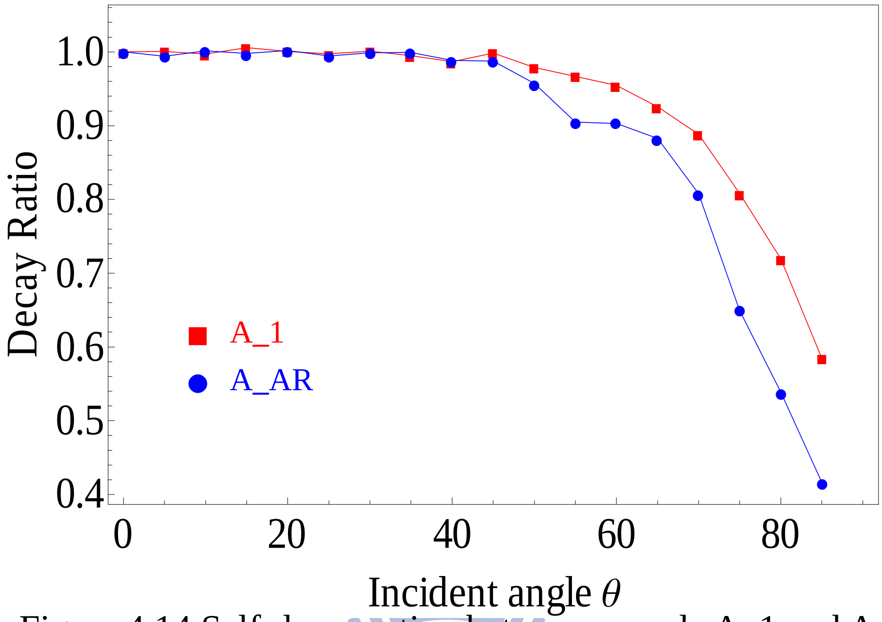

Figure 4.14 Self-decay ration between sample A_1 and A_AR

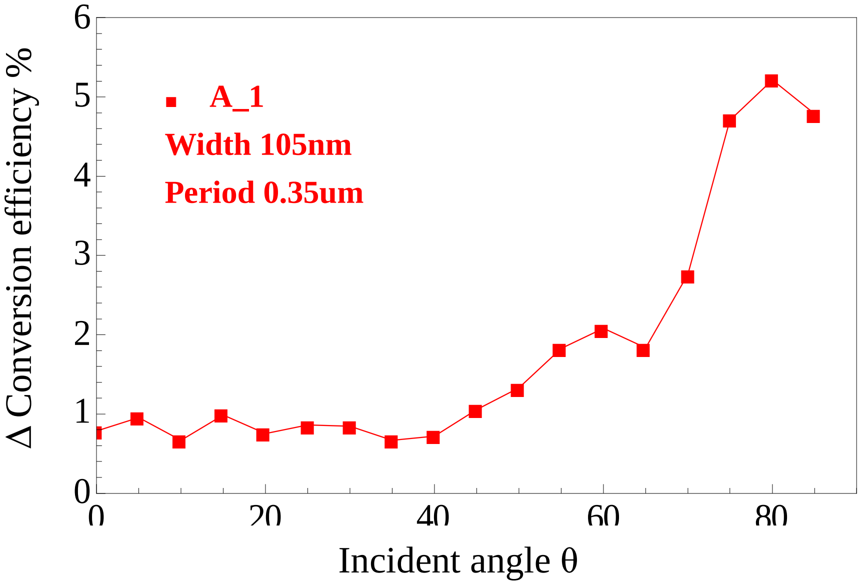

Figure 4.15 Measured efficiency difference between A_1 and A_AR along different incident angle

### Dependency of filling factor

In this study, we also design grating with various width from 100 nm to 150 nm, corresponding to filling factor 0.3 to 0.5. The devices B_2 and C_2 listed in Table 1.1 which designed for larger grating width, 140nm and 150nm, respectively, indicate to have relatively low efficiency. In theoretical calculation shown in figure 4.16, with grating of period 0.35 μm and depth 0.1 μm, TSolar transmittance indicates a maximum at filling factor 0.3. In addition, the transmittance descends gradually from 95.5% to 94.5% on both large and small filling factor. In the meanwhile, the efficiency dependence on incident angle is also considered. As a result, the same comparison according to figure 4.15 is done and show in figure 4.17. Figure 4.17 (a) and (b) are the results of sample B and C, respectively. Although the efficiency of B_2 and C_2 are slightly less than B_AR and C_AR at normal incident, the curves begin to dominate at larger incidence. Both curves in each plot indicate similar tendency that also B_2 and C_2 present less increment compared to B_1 and C_1.

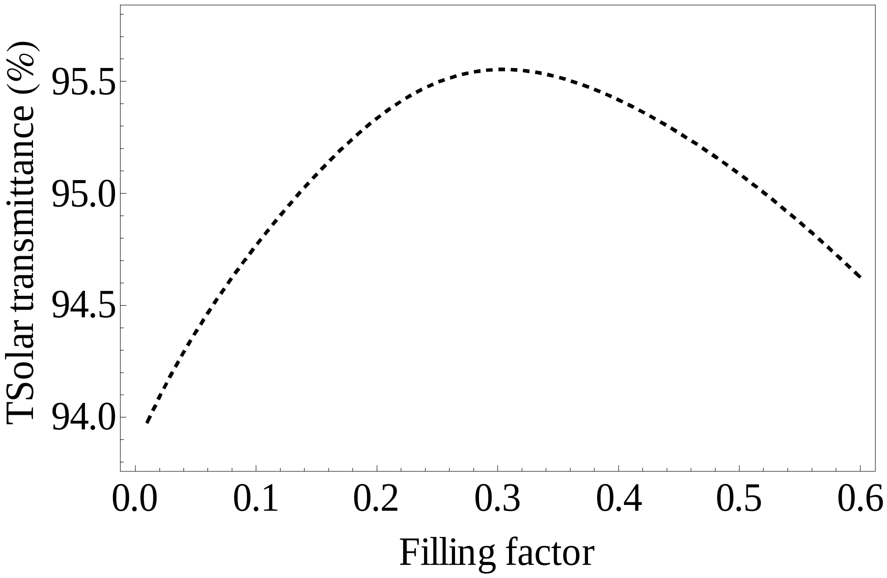

Figure 4.16 Tsolar as function of filling factor at normal incidence

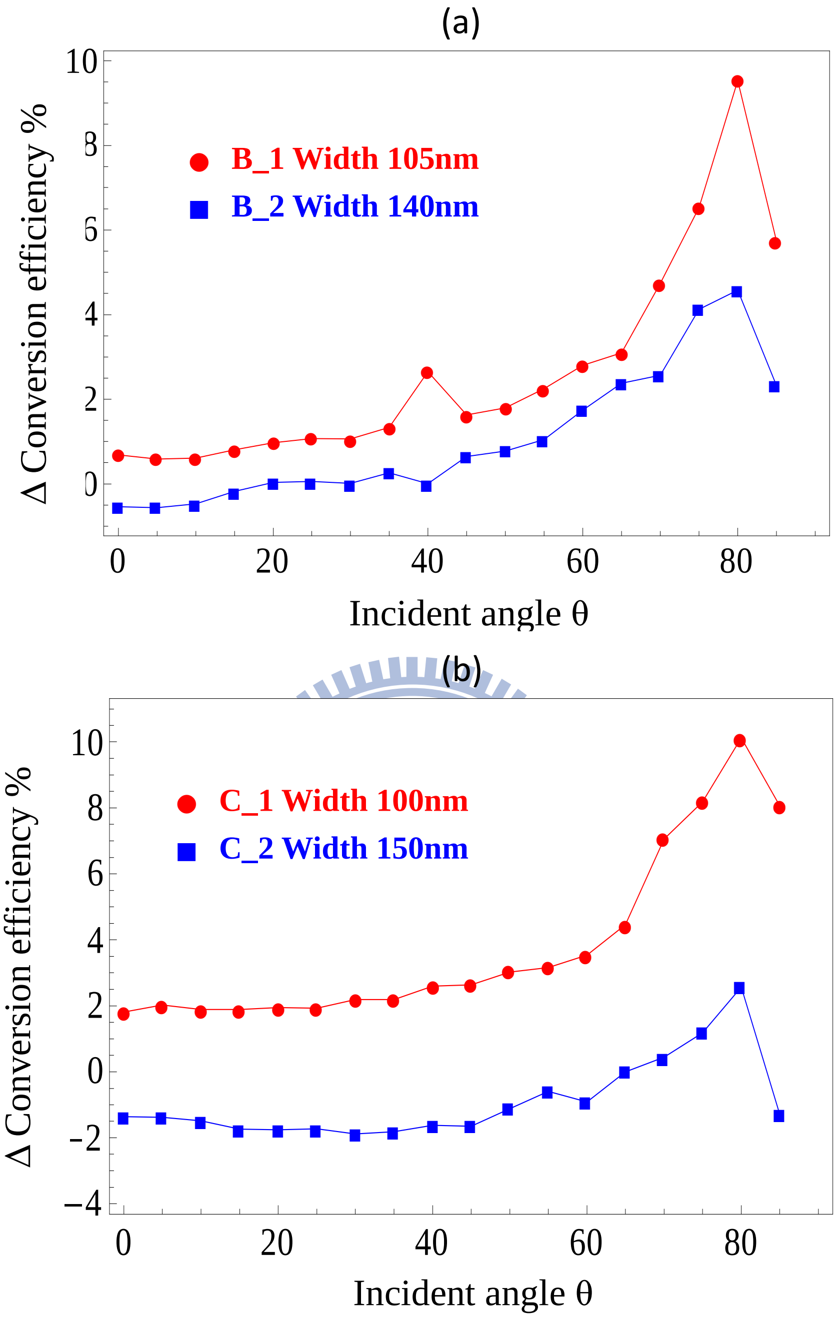

Figure 4.17 Measured efficiency differences along different incident angle of (a) device B and (b) device C.

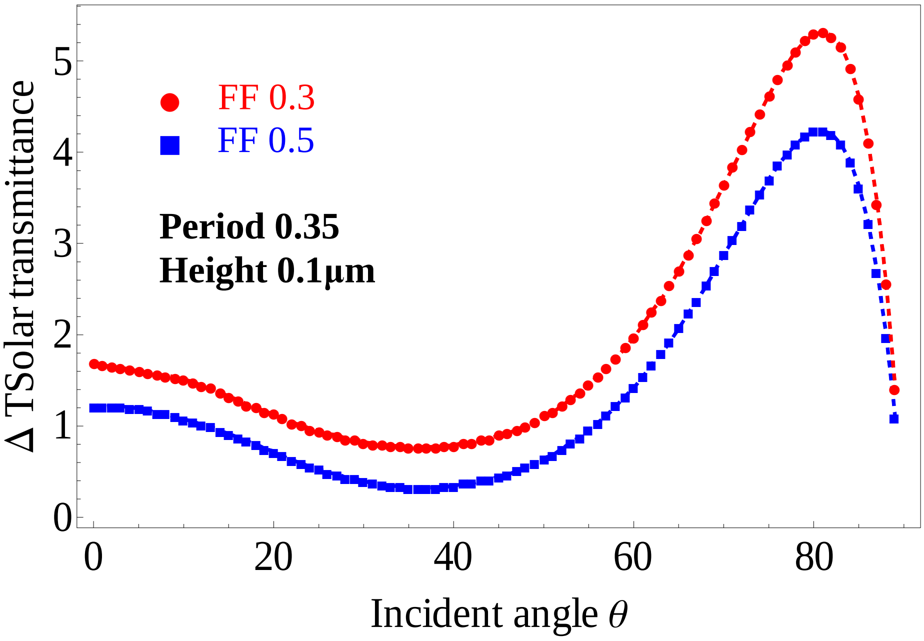

Figure 4.18 Simulation of TSolar differences for different filling factor along different incident angle

Figure 4.18 is a simulation by calculating TSolar transmittance subtraction between different filling factor and AR. In which we notice that grating with narrower width, smaller filling factors, has better performance at larger incidence. Even though efficiency relation to TSolar transmittance can not be told categorically, we are surprise to find the good qualitative agreement of figure 4.17 with figure 4.18. We can also imply that the improvement of efficiency comes from the raised amount of photon penetrating through surface which finally contributes to the total photon current density and total power output.

,

## 4.3 Discussion

### Wavelength distribution at different angle of incidence

Figure 4.19 is the comparison of changing transmittance distribution of wavelength 0.3μm to 2μm at increasing incident angle from normal to level. Graph (a) shows the surface with grating and AR, and graph and (b) with only AR at the front. Apparetnly, they all have two regions where wavelength around 0.5μm and 0.8μm achieve high transmittance. Fortunately, these two peaks barely shift away along larger incident angle. However, graph (a) indicates slower decrement throughout whole span and the phenomenon becomes more obvious after 60 degree of incidence, over 5% higher than graph (b) at 0.8μm. The much less amount of photon dissipated at oblique incidence contributes to the step up trend in figure 4.18 and maybe explain the same situation appears in

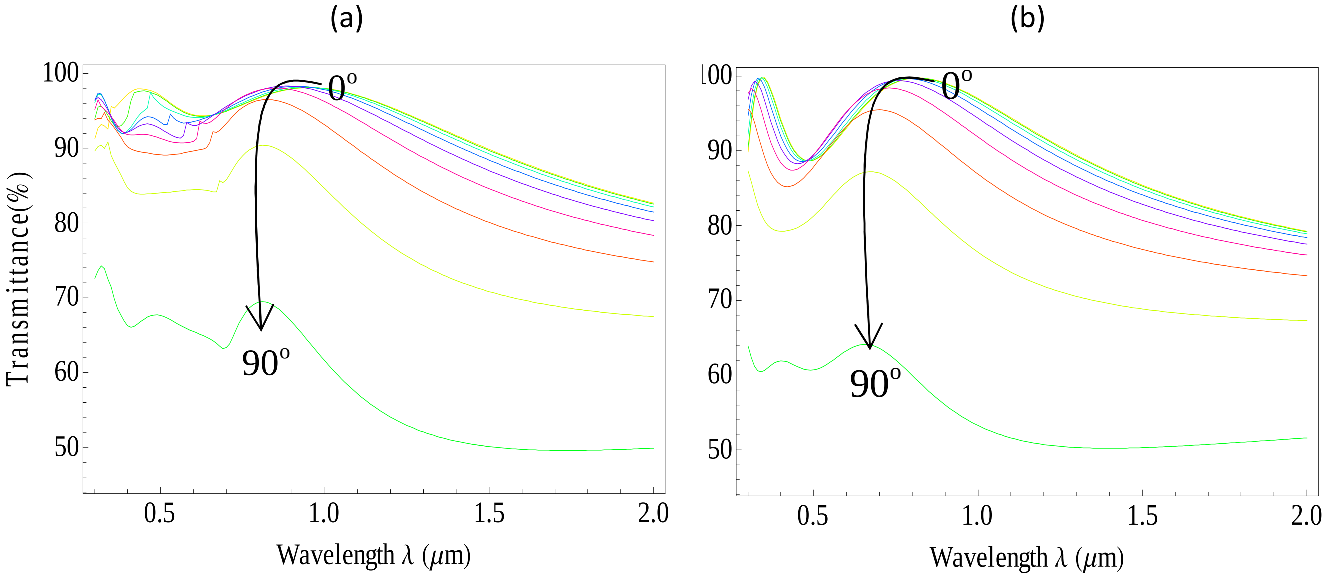

Figure 4.19 The transmittance comparison of wavelength distribution of surface with (a) grating structure on AR (b) AR at increasing angle of incidence, along the arrow.

our experiment. Moreover, another advantage of grating structure is one of its maximum at short wavelength 0.5μm is closer to the main peak of solar spectrum, 0.4~0.7um, and move even closer at large incident angle which compensate the reflectivity loss happened on graph (b). Consequently, sample with the help of light trapping mechanism presents more efficient photon attraction and shows out higher efficiency.

**Error deviation**

The experiment deviation could be resulted from the inherit fluctuation of beam source within 1mm square size of devices which cause ±1% variation and irregular rise and fall when plotting. Although efficiency with grating may be sometimes lower than expected, it is more important to focus on the relative tendency between interested and reference samples.

The mechanical damages are sometimes avoidable during circuit mounting and device isolation by using scriber. These uncertainties may bring out problems like short circuit, current leakage; larger shunt resistances and junction skip. Junction skip is generally caused when too many defects built up a bypass, and normally can be detect by the diminished turn-on voltage.

Additionally, the rotation apparatus we set up to adjust the angle of solar simulator impinging on device is uni-axle. And 1-D grating is an angle dependent structure, the diffraction effect results differently depends on the direction it rotates. Therefore, we have to make sure that grating is lined up along the same axle, which in general can only be rectified by hand.

The exact functionalities that contribute to final efficiency after taking all disturbances either intrinsic or exterior into account is far more complicated.

Some of parameters can be extracted by certain commercial software, which is beyond our interest. However, if we can check the essential electrical properties, turn-on voltage and I-V tendency, carefully before each measurement, some of error deviations can still be avoided and eliminated.

# Chapter 5

# Conclusion

In this study, the antireflection and light trapping effects of 1-D sub-wavelength grating were quantitatively investigated by means of numerical simulation, RCWA. It indicates the reflection loss can be reduced by the characteristic of grating over a wide range of wavelength. We then realized our idea onto III-V MJ solar cells and compared the short circuit current density and efficiency to device without grating over wide incident angle in order to observe the effect. Eventually, higher efficiency and current density at normal incidence and less decrement at oblique incidence were found. Although it is not apprent to conclude the cause and effect between efficiency to amount of photon transmitted, by measuring the quantum efficiency of each subcell among responsive wavelength, it is straightforward to observe the effect of number of photon increment to the higher short circuit current density. Moreover, we are glad to notice the experimental curves roughly follow the trend of theoretical calculation between the subtraction of TSolar transmittance to surface with and without grating. Thus we can conclude that the increment of power conversion efficiency over wide incidence can be credited to the enhancement of photon collection due to the photon trapping design of sub-wavelength grating.

### Future work

Sub-wavelength gratings have its advantage of being a light pass filter on the surface, however, the disadvantage is the fact that its rather difficult to fabricate size that make E-Beam lithography technique hard to offer a rapid replication under scale of micrometer in mass production. Embossing, interferometric lithography have been studied [7] but still worth further investigation. Accordingly, if there exist other more feasible and less costly methods to pattern such periodic structure, it could be widely extended in the aspect of either terrestrial or spatial applications.

## *Reference*

[1] W. Shockley, H.J. Queisser, “Detailed Balance Limit of Efficiency of p-n Junction Solar Cells”, J. Appl. Phys, **32**, 510-519(1961)

[2] M. Yamaguchi, K. Nishimura, T. Sasaki, “Novel materials for high efficiency III-V multi-junction solar cells”, Solar Energy, **82**, 173-180( 2008)

[3] Y.G. Xiao, Z.Q. Li, Z.M. Simon Li, “Modeling of GaInP/GaAs/Ge and the inverted-grown metamorphic GaInP/GaAs/GaInAs triple-junction solar cells” Proc. Of SPIE, **7041,** 70430B(2008)

[4] R.R. King, D.C. Law, K.M. Edmondson, “40% efficient metamorphic GaInP/GaInAs/Ge multijunction solar cells”, Appl. Phys Lett., **90**, 183516( 2007)

[5] W. Zhou, M. Tao, L. Chen, “Microstructured surface design for omnidirectional antireflection coatings on solar cells”, J. Appl. Phys., **102**,103105(2007)

[6] J.Q. Xi, M.F. Schubert, J.K. Kim, “Optical thin-film materials with low refractive index for broadband elimination of Fresnel reflection”, Nature Photonics, **1**, 176-179( 2007)

[7] S.H. Zaidi, J.M. Gee, D.S. Ruby, “Diffraction grating structures in solar cells”, IEEE Photovoltaic Specialists Conference, **28**,395(2000)

[8] N. Senoussaoui, M. Krause, J. Müller, “Thin-film solar cells with periodic grating coupler“ Thin solid films, **451-452,** 397-401(2004)

[9] A. Gombert, K. Rose, A. Heinzel, “Antireflective submicrometer surface-relief gratings for solar applications”, Solar Energy Materials and Solar Cells, **54**, 333-342(1998)

[10] C. Heine, R.H. Morf, “Submicrometer gratings for solar energy applications”, Appl. Opt., **34**, 2476-2482(1995)

[11] H. Sai, Y. Kanamori, K. Arafune, “Light trapping effect of submicron surface textures in crystalline Si solar cells”, Prog. Photovolt. Res. Appl, **15,** 415-423(2007)

[12] T.K. Gaylord, M.G. Moharam “Analysis and Application of Optical Diffraction by Gratings” Proceedings of The IEEE, **73,** 894-924(1985)

[13] K. Hirayama, E.N. Glytsis, T.K. Gaylord, “Rigorous electromagnetic analysis of diffraction by finite-number-periods gratings”, J. Opt. Soc. Am. A, **14**,907-917(1997)

[14] M.G. Moharam, D.A. Pommet, E.B. Grann, T.K. Gaylord, “Stable implementation of rigorous coupled-wave analysis for surface-relief gratings: enhanced transmittance matrix approach” J. Opt. Soc. Am. A., **12**, 1077-1086(1995)

[15] M.G. Moharam, D.A. Pommet, E.B. Grann, T.K. Gaylord, “Formulation for stable ad efficient implementation of rigorous coupled-wave analysis of binary gratings”, J. Opt.

Soc. Am A, **12**,1068-1076(1995)

[16] D,A, Neamen "Semiconductor physics and devices", Mc Graw Hill, 3rd(2003)

[17] Jenny Nelson, "The physics of solar cells", Imperial College Press(2003)

[18] Erees Q.B. Macabebe, E. Ernest van Dyk, "Parameter extraction from dark current-voltage characteristics of solar cells", South Africa J. Sci., **104**, 401-404(2008)

[19] B. Galiana, C. Algora, I. Rey-Stolle, "Explanation for the Dark I-V Curve of III-V concentrator solar cells", Prog. Photovolt: Res. Appl., **16**, 331-338(2008)

[20] G. Conibeer, R. Patterson, L. Huang, "Modeling of hot carrier solar cell absorbers", Solar Energy Material & Solar Cells, **94**, 1516-1521(2010)

[21] L.M. Fraas, G.R, Girard, J.E, Avery, "GaSb booster cells for over 30% efficient solar-cell stacks" J. Appl. Phys. **66**, 3866(1989)

[22] M. Yamaguchi, "III-V compound multi-junction solar cells: present and futre", Solar energy materials & Solar Cells, **75,** 261-269(2003)

[23] M. Yamaguchi, "Multi-junction solar cells and novel structures for solar cell applications", Phyica E, **14**, 84-90(2002)

[24] D.L. Brundrett, E.N. Glytsis, and T.K. Gaylord, "Homogeneous layer models for high-spatial-frequency dielectric surface-relief gratings conical diffraction and antireflection designs" Applied Opt. **33,** 2695-2706(1994)

[25] H. Stiebig, N. Senoussaoui, C. Zahren "Silicon Thin-film solar cells with rectangular-shaped grating couplers", Prog. Photovolt. Res. Appl, **14**, 13-24, 2006

[26] D.M. Pai, K.A. Awada, "Analysis of dielectric gratings of arbitrary profiles and thicknesses", J. Opt. Soc. Am. A, **8,** 755-762(1991)

[27] D.J. Griffiths, "Introduction to electrodynamics", Prentice Hall, 3rd(1999)

[28] K. Nishioka, T. Takamoto, T. Agui, "Evaluation of InGaP/InGaAs/Getriple-junction solar cell and optimization of solar cell's structure focusing on series resistance for high efficiency concentrator photovoltaic systems" Solar Energy Materials and Solar Cells, **90**, 1308-1321(2006)

[29] M. Zaknoune, O. Schuler, F. Mollot, "Nonselective wet chemical etching of GaAs and AlGaInP for device applications", J. Vac. Sci.Technol. B, **16(1)**, 223-226(1998)

[30] M.H. Merbah, M. Belhamel, I. Tobias, "Extraction and analysis of solar parameters from the illuminated current-voltage curve", Solar Energy Materials and Solar Cells, **87**, 225-233(2005)

# Appendix A

## *TM Partial Solution For Reflection*

$$\begin{pmatrix} W_L X_L & W_L \\ V_L X_L & -V_L \end{pmatrix}\begin{pmatrix} C_L^+ \\ C_L^- \end{pmatrix} = \begin{pmatrix} I \\ jZ_{II} \end{pmatrix} T$$

$$\rightarrow \begin{pmatrix} -W_L & I \\ V_L & jZ_{II} \end{pmatrix}\begin{pmatrix} C_L^- \\ T \end{pmatrix} = \begin{pmatrix} W_L X_L \\ V_L X_L \end{pmatrix} C_L^+$$

$$\rightarrow \begin{pmatrix} C_L^- \\ T \end{pmatrix} = \begin{pmatrix} -W_L & I \\ V_L & jZ_{II} \end{pmatrix}^{-1}\begin{pmatrix} W_L X_L \\ V_L X_L \end{pmatrix} C_L^+$$

$$f_0 = I \, ; \, g_0 = jZ_{II} \, ; \, \begin{pmatrix} a_L \\ b_L \end{pmatrix} = \begin{pmatrix} -W_L & I \\ V_L & jZ_{II} \end{pmatrix}^{-1}\begin{pmatrix} W_L X_L \\ V_L X_L \end{pmatrix} C_L^+ \, ; C_{L+1}^+ = T \, ;$$

$$\rightarrow \begin{pmatrix} C_L^- \\ C_{L+1}^+ \end{pmatrix} = \begin{pmatrix} a_L \\ b_L \end{pmatrix} C_L^+$$

$$\rightarrow \begin{cases} C_L^- = a_L C_L^+ \\ C_{L+1}^+ = b_L C_L^+ \end{cases} \text{substitude into} \begin{pmatrix} W_L & W_L X_L \\ V_L & -V_L X_L \end{pmatrix}\begin{pmatrix} C_L^+ \\ C_L^- \end{pmatrix} \text{we can obtain}$$

$$\rightarrow \begin{pmatrix} W_L & W_L X_L \\ V_L & -V_L X_L \end{pmatrix}\begin{pmatrix} I \\ a_L \end{pmatrix} C_L^+ = \begin{pmatrix} W_L (I + X_L a_L) \\ V_L (I - V_L a_L) \end{pmatrix} C_L^+$$

$$f_L = W_L (I + X_L a_L) \; ; \; g_L = V_L \, (I - V_L a_L)$$

$$\rightarrow \begin{pmatrix} W_L & W_L X_L \\ V_L & -V_L X_L \end{pmatrix}\begin{pmatrix} C_L^+ \\ C_L^- \end{pmatrix} = \begin{pmatrix} f_L \\ g_L \end{pmatrix} C_L^+$$

Repeat the process again and again we can then obtain

$$\rightarrow \begin{cases} 1. \begin{pmatrix} W_{l-1} X_{l-1} & W_{l-1} \\ V_{l-1} X_{l-1} & -V_{l-1} \end{pmatrix}\begin{pmatrix} C_{l-1}^+ \\ C_{l-1}^- \end{pmatrix} = \begin{pmatrix} f_l \\ g_l \end{pmatrix} C_l^+ \text{ deduce that } \begin{pmatrix} W_l & W_l X_l \\ V_l & -V_l X_l \end{pmatrix}\begin{pmatrix} C_l^+ \\ C_l^- \end{pmatrix} = \begin{pmatrix} f_l \\ g_l \end{pmatrix} C_l^+ \\ 2. \;\; f_l = W_l (I + X_l a_l) \; ; \; g_l = V_l (I - V_l a_l) \\ 3. \begin{pmatrix} a_l \\ b_l \end{pmatrix} = \begin{pmatrix} -W_l & I \\ V_l & jZ_{II} \end{pmatrix}^{-1}\begin{pmatrix} W_l X_l \\ V_l X_l \end{pmatrix} \end{cases}$$

Finally we get the following results

$$\rightarrow \begin{pmatrix} W_1 X_1 & W_1 \\ V_1 X_1 & V_1 \end{pmatrix}\begin{pmatrix} C_1^+ \\ C_1^- \end{pmatrix} = \begin{pmatrix} f_2 \\ g_2 \end{pmatrix} C_2^+$$

$$\rightarrow \begin{pmatrix} W_1 & W_1 X_1 \\ V_1 & -V_1 X_1 \end{pmatrix}\begin{pmatrix} C_1^+ \\ C_1^- \end{pmatrix} = \begin{pmatrix} f_1 \\ g_1 \end{pmatrix} C_1^+ = \begin{pmatrix} \delta_{io} \\ j \dfrac{\delta_{i0} \cos\theta}{n_I} \end{pmatrix} + \begin{pmatrix} I \\ -jZ_I \end{pmatrix} R$$

### *TM Partial Solution for Transmission*

$$\begin{pmatrix} \delta_{i0} \\ j\dfrac{\delta_{i0}\cos\theta}{n_I} \end{pmatrix} + \begin{pmatrix} I \\ -jZ_I \end{pmatrix} R = \begin{pmatrix} W_1 & W_1X_1 \\ V_1 & -V_1X_1 \end{pmatrix} \begin{pmatrix} C_1^+ \\ C_1^- \end{pmatrix}$$

$$\rightarrow \begin{pmatrix} -W_1X_1 & I \\ V_1X_1 & -jZ_I \end{pmatrix} \begin{pmatrix} C_1^- \\ C_0^+ \end{pmatrix} = \begin{pmatrix} W_1 \\ V_1 \end{pmatrix} C_1^+ - \begin{pmatrix} \delta_{i0} \\ j\dfrac{\delta_{i0}\cos\theta}{n_I} \end{pmatrix}$$

$$f_0 = I \; ; \; g_0 = -jZ_I \; ; \; y_0 = \delta_{i0} \; ; \; z_0 = j\frac{\delta_{i0}\cos\theta}{n_I} \; ; \; R = C_0^+$$

$$\rightarrow \begin{pmatrix} C_1^- \\ C_0^+ \end{pmatrix} = \begin{pmatrix} -W_1X_1 & f_0 \\ V_1X_1 & g_0 \end{pmatrix}^{-1} \begin{pmatrix} W_1 \\ V_1 \end{pmatrix} C_1^+ - \begin{pmatrix} -W_1X_1 & f_0 \\ V_1X_1 & g_0 \end{pmatrix}^{-1} \begin{pmatrix} y_0 \\ z_0 \end{pmatrix}$$

$$L_1 = \begin{pmatrix} -W_1X_1 & f_0 \\ V_1X_1 & g_0 \end{pmatrix}^{-1} \; ; \; \begin{pmatrix} a_1 \\ b_1 \end{pmatrix} = L_1 \begin{pmatrix} W_1 \\ V_1 \end{pmatrix} \; ; \; \begin{pmatrix} m_1 \\ n_1 \end{pmatrix} = L_1 \begin{pmatrix} y_0 \\ z_0 \end{pmatrix}$$

$$\rightarrow \begin{pmatrix} C_1^- \\ C_0^+ \end{pmatrix} = \begin{pmatrix} a_1 \\ b_1 \end{pmatrix} C_1^+ - \begin{pmatrix} m_1 \\ n_1 \end{pmatrix}$$

$$\rightarrow \begin{cases} C_1^- = a_1C_1^+ - m_1 \\ C_0^+ = b_1C_1^+ - n_1 \end{cases}$$

$C_1^-$ substitude back to $\begin{pmatrix} W_1X_1 & W_1 \\ V_1X_1 & -V_1 \end{pmatrix} \begin{pmatrix} C_1^+ \\ C_1^- \end{pmatrix}$

$$\rightarrow \begin{pmatrix} W_1(X_1+a_1) \\ V_1\,(X_1-a_1) \end{pmatrix} C_1^+ + \begin{pmatrix} -W_1 \\ V_1 \end{pmatrix} m_1$$

$$f_1 = W_1(X_1+a_1) \; ; \; g_1 = V_1\,(X_1-a_1) \; ; \; y_1 = -W_1m_1 \; ; \; z_1 = V_1m_1$$

$$\rightarrow \begin{pmatrix} W_1(X_1+a_1) \\ V_1\,(X_1-a_1) \end{pmatrix} C_1^+ + \begin{pmatrix} -W_1 \\ V_1 \end{pmatrix} m_1 = \begin{pmatrix} f_1 \\ g_1 \end{pmatrix} C_1^+ + \begin{pmatrix} y_1 \\ z_1 \end{pmatrix} = \begin{pmatrix} W_1X_1 & W_1 \\ V_1X_1 & -V_1 \end{pmatrix} \begin{pmatrix} C_1^+ \\ C_1^- \end{pmatrix}$$

$$\therefore \begin{pmatrix} W_2 & W_2X_2 \\ V_2 & -V_2X_2 \end{pmatrix} = \begin{pmatrix} f_1 \\ g_1 \end{pmatrix} C_1^+ + \begin{pmatrix} y_1 \\ z_1 \end{pmatrix}$$

*R*epeat the process again and again then you can derive that

$$\rightarrow \begin{cases} 1. \; \begin{pmatrix} W_{l+1} & W_{l+1}X_{l+1} \\ V_{l+1} & -V_{l+1}X_{l+1} \end{pmatrix} \begin{pmatrix} C_{l+1}^+ \\ C_{l+1}^- \end{pmatrix} = \begin{pmatrix} f_l \\ g_l \end{pmatrix} C_l^+ + \begin{pmatrix} y_l \\ z_l \end{pmatrix} \text{ deduce that } \begin{pmatrix} W_lX_l & W_l \\ V_lX_l & -V_l \end{pmatrix} \begin{pmatrix} C_l^+ \\ C_l^- \end{pmatrix} = \begin{pmatrix} f_l \\ g_l \end{pmatrix} C_l^+ + \begin{pmatrix} y_l \\ z_l \end{pmatrix} \\ 2. \; f_n = W_n(X_n+a_n) \; ; \; g_n = V_n(X_n-a_n) \\ 3. \; y_n = -W_nm_n \; ; \; z_n = V_nm_n \end{cases}$$

Finally we obtain the following results

$$\rightarrow \begin{pmatrix} W_{L-1}X_{L-1} & W_{L-1} \\ V_{L-1}X_{l-1} & V_{L-1} \end{pmatrix} \begin{pmatrix} C_{L-1}^+ \\ C_{L-1}^+ \end{pmatrix} = \begin{pmatrix} f_{L-1} \\ g_{L-1} \end{pmatrix} C_{L-1}^+ + \begin{pmatrix} y_{L-1} \\ z_{L-1} \end{pmatrix} = \begin{pmatrix} W_L & W_LX_L \\ V_L & -V_LX_L \end{pmatrix} \begin{pmatrix} C_L^+ \\ C_L^- \end{pmatrix}$$

$$\rightarrow \begin{pmatrix} W_LX_L & W_L \\ V_LX_L & -V_L \end{pmatrix} \begin{pmatrix} C_L^+ \\ C_L^- \end{pmatrix} = \begin{pmatrix} f_L \\ g_L \end{pmatrix} C_L^+ + \begin{pmatrix} y_L \\ z_L \end{pmatrix} = \begin{pmatrix} I \\ jZ_{II} \end{pmatrix} T$$